IMAGING ELECTRICAL CONDUCTIVITY DISTRIBUTION OF THE HUMAN HEAD USING EVOKED FIELDS AND POTENTIALS

A THESIS SUBMITTED TO
THE GRADUATE SCHOOL OF NATURAL AND APPLIED SCIENCES
OF
MIDDLE EAST TECHNICAL UNIVERSITY

BY

MUSTAFA YURTKÖLESİ

IN PARTIAL FULFILLMENT OF THE REQUIREMENTS
FOR
THE DEGREE OF MASTER OF SCIENCE
IN
ELECTRICAL AND ELECTRONICS ENGINEERING

SEPTEMBER 2008

Approval of the thesis:

IMAGING ELECTRICAL CONDUCTIVITY DISTRIBUTION OF THE HUMAN HEAD USING EVOKED FIELDS AND POTENTIALS

submitted by **MUSTAFA YURTKÖLESİ** in partial fulfillment of the requirements for the degree of
Master of Science in Electrical and Electronics Engineering Department, Middle East Technical University by,

Prof. Dr. Canan Özgen
Dean, Graduate School of **Natural and Applied Sciences** ______________

Prof. Dr. İsmet Erkmen
Head of Department, **Electrical and Electronics Engineering** ______________

Prof. Dr. Nevzat G. Gençer
Supervisor, **Electrical and Electronics Engineering Department, METU** ______________

Examining Committee Members:

Prof. Dr. Murat Eyüboğlu
Electrical and Electronics, METU ______________

Prof. Dr. Nevzat G. Gençer
Electrical and Electronics, METU ______________

Prof. Dr. Kemal Leblebicioğlu
Electrical and Electronics, METU ______________

Prof. Dr. Ergin Atalar
Electrical and Electronics, Bilkent University ______________

Assist. Prof. Dr. Yeşim Serinağaoğlu
Electrical and Electronics, METU ______________

Date: ______________

I hereby declare that all information in this document has been obtained and presented in accordance with academic rules and ethical conduct. I also declare that, as required by these rules and conduct, I have fully cited and referenced all material and results that are not original to this work.

Name, Last Name: MUSTAFA YURTKÖLESİ

Signature :

ABSTRACT

IMAGING ELECTRICAL CONDUCTIVITY DISTRIBUTION OF THE HUMAN HEAD USING EVOKED FIELDS AND POTENTIALS

Yurtkölesi, Mustafa
M.S., Department of Electrical and Electronics Engineering
Supervisor : Prof. Dr. Nevzat G. Gençer

September 2008, 82 pages

In the human brain, electrical activities are created due to the body functions. These electrical activities create potentials and magnetic fields which can be monitored electrically (Electroencephalography - EEG) or magnetically (Magnetoencephalography - MEG). Electrical activities in human brain are usually modeled by electrical dipoles. The purpose of Electro-magnetic source imaging (EMSI) is to determine the position, orientation and strength of dipoles. The first stage of EMSI is to model the human head numerically. In this study, The Finite Element Method (FEM) is chosen to handle anisotropy in the brain. The second stage of EMSI is to solve the potentials and magnetic fields for an assumed dipole configuration (forward problem). Realistic conductivity distribution of human head is required for more accurate forward problem solutions. However, to our knowledge, conductivity distribution for an individual has not been computed yet.

The aim of this thesis study is to investigate the feasibility of a new approach to update the initially assumed conductivity distribution by using the evoked potentials and fields acquired during EMSI studies. This will increase the success of source localization problem, since more realistic conductivity distribution of the head will be used in the forward problem. This new method can also be used as a new imaging modality, especially for inhomogeneities where the conductivity value deviates.

In this thesis study, to investigate the sensitivity of measurements to conductivity perturbations, a FEM based sensitivity matrix approach is used. The performance of the proposed method is tested using three different head models - homogeneous spherical, 4 layer concentric sphere and realistic head model. For spherical head models rectangular grids are preferred in the middle and curved elements are used nearby the head boundary. For realistic cases, head models are developed using uniform grids. Tissue boundary information is obtained by applying segmentation algorithms to the Magnetic Resonance (MR) images. A paralel computer cluster is employed to assess the feasibility of this new approach. PETSc library is used for forward problem calculations and linear system solutions.

The performance of this novel approach depends on many factors such as the head model, number of dipoles and sensors used in the calculation, noise in the measurements, etc. In this thesis study, a number of simulations are performed to investigate the effects of each of these parameters. Increase in the number of elements in the head model leads to the increase in the number of unknows for linear system solutions. Then, accuracy of the solution is improved with increased number of dipoles or sensors. The performance of the adopted approach is investigated using noise-free measurements as well as noisy measurements. For EEG, measurement noise decreases the accuracy of the approach. For MEG, the effect of measurement noise is more pronounced and may lead to a larger error in tissue conductivity calculation.

Keywords: EEG, MEG, EMSI, Evoked Fields And Potentials, Forward Problem

ÖZ

İNSAN KAFASI ELEKTRİKSEL İLETKENLİK DAĞILIMININ UYARILMIŞ ALANLAR VE POTANSİYELLER İLE GÖRÜNTÜLENMESİ

Yurtkölesi, Mustafa
Yüksek Lisans, Elektrik ve Elektronik Mühendisliği Bölümü
Tez Yöneticisi : Prof. Dr. Nevzat G. Gençer

Eylül 2008, 82 sayfa

İnsan beyninde vücut fonksiyonlarına bağlı olarak elektriksel aktiviteler meydana gelmektedir. Bu elektriksel aktivitelerin yarattığı potansiyeller ve manyetik alanlar, elektriksel (Elektroensefalografi - EEG) ve manyetiksel (Magnetoensefalografi - MEG) yöntemler ile gözlemlenebilir. İnsan beynindeki elektriksel aktiviteler, elektrik dipolleri ile modellenmektedir. Elektromanyetik kaynak görüntülemenin (EMKG) amacı bu dipollerin yer, yön ve şiddetini belirlemektir. EMKG'nin ilk aşaması insan kafasını sayısal olarak modellemektir. Bu çalışmada, Sonlu Elemanlar Yöntemi (SEY) beyindeki yönbağımlılıkla başa çıkmak için seçilmiştir. EMKG'nin ikinci aşaması, varsayılan dipol konfigürasyonu için potansiyelleri ve manyetik alanları çözmektedir (ileri problem). İnsan kafasının gerçekçi iletkenlik dağılımı, daha doğru ileri problem çözümleri için gereklidir. Ama, bizim bildiğimiz kadarıyla bir birey için iletkenlik dağılımı henüz hasaplanmış değildir.

Bu tez çalışmasının amacı, varsayılan başlangıç iletkenlik dağılımını güncellemek için, EMKG çalışmalarından elde edilen uyarılmış potansiyeller ve alanları kullanan yeni

bir yaklaşımın olurluğunu incelemektir. Bu, ileri problemde beynin gerçekçi iletkenlik dağılımı kullanılacağı için, kaynak konumlama problemindeki başarı oranını arttıracaktır. Bu yeni metod aynı zamanda beyin iletkenlik dağılımının farklılaştığı bölgelerin görüntülenmesi için de kullanılabilecektir.

Ölçümlerin, iletkenlikteki farklılaşmalara olan duyarlılığını incelemek için SEY tabanlı duyarlılık matrisi yaklaşımı kullanılmıştır. Önerilen yöntemin performansı üç farklı kafa modeli - homojen küre, 4 kabuklu konsentrik küre ve gerçekçi kafa modeli - kullanılarak test edilmiştir. Küresel kafa modelleri için ortalarda dikdörtgensel şebekeler tercih edilmiş, kafa sınırı yakınlarında eğri elemanlar kullanılmıştır. Gerçekçi durumlar için, kafa modelleri birbiçimli şebekeler kullanılarak oluşturulur. Doku sınır bilgisi, Manyetik Rezonans (MR) görüntülerine uygulanan bölütleme algoritmaları ile elde edilmiştir. Bu yeni metodu gerçeklemek için paralel bilgisayar kümesi görevlendirilmiştir. İleri problem hesaplamaları ve doğrusal sistem çözümleri için PETSc kütüphanesi kullanılmıştır.

Bu özgün yaklaşımın performansı kafa modeli, hesaplamalarda kullanılan dipollerin ve sensörlerin sayısı, ölçümlerdeki gürültü ve bu gibi çok sayıda faktöre bağlıdır. Bu tez çalışmasında, bu parametrelerden herbirinin etkisini gözlemlemek için simülasyonlar gerçekleştirilmiştir. Kafa modelindeki eleman sayısı artış, doğrusal sistem çözümlerindeki bilinmeyen sayısında artışa neden olur. O zaman, çözümün doğruluğu dipol ve sensör sayısındaki artışla birlikte geliştirilir. Benimsenen yaklaşımın performansı gürültüsüz ölçümlerle birlikte gürültülü ölçümler kullanarak da gözlenmiştir. EEG için, ölçüm gürültüsü yaklaşımın doğruluğunu azaltır. MEG için, ölçüm gürültüsünün etkisi daha belirgindir ve doku iletkenlik hesaplarında daha büyük hataya neden olur.

Anahtar Kelimeler: EEG, MEG, EMKG, İleri Problem, Uyarılmış Alanlar Ve Potansiyeller

ACKNOWLEDGMENTS

I would like to thank my supervisor Prof. Dr. Nevzat Gençer for his guidence. I also wish to thank Dr. Can E. Acar for software and data provided by him. I also wish to thank Yoldaş Ataseven for his support at parallel programming.

TABLE OF CONTENTS

ABSTRACT iv

ÖZ vi

ACKNOWLEDGMENTS viii

TABLE OF CONTENTS ix

LIST OF TABLES xi

LIST OF FIGURES xiii

CHAPTERS

1 INTRODUCTION 1

1.1 General Overview 1

1.2 Objective of the Study 2

1.3 Significance of the Study 3

1.4 Outline of the Thesis 3

2 IMAGING THE CONDUCTIVITY DISTRIBUTION OF THE HUMAN HEAD 4

2.1 Introduction 4

2.2 Sensitivity of EEG and MEG measurements to tissue conductivities 8

2.3 Procedure 11

3 RESULTS 14

3.1 Introduction 14

3.2 Homogenous Sphere 14

3.2.1 Reconstructing the conductivity distribution of a homogeneous sphere 16

3.2.2 Effects of the number of measurements on the condition number 17

3.2.3 Contrast Resolution 20
3.2.4 Effects of Dipole Orientation 24
3.2.5 Dipole with varying orientations 28
3.3 Concentric Sphere 30
3.3.1 Computing Tissue Conductivities of the four-layer head model (4 unknowns) 31
3.3.2 Reconstructing the conductivity distribution of the four-layer head model (Many unknowns) 33
3.3.3 Inhomogeneity Imaging 35
3.4 Realistic Head Model 49
3.4.1 Computing Tissue Conductivities of the realistic head model (4 unknowns) 50
3.4.2 Reconstructing the conductivity distribution of the realistic head model - Many unknowns 52
3.4.3 Inhomogeneity Imaging 53
4 CONCLUSION AND DISCUSSION 67
4.1 Conclusion 67
4.1.1 Effect of the Number of Measurements 67
4.1.2 Contrast Resolution 68
4.1.3 Computing Tissue Conductivities (4 unknowns) . . . 68
4.1.4 Reconstructing the conductivity distribution (Many unknowns) 69
4.1.5 Inhomogeneity Imaging 69
4.2 Discussion 70
REFERENCES 72
APPENDICES
APPENDICES
A FORWARD PROBLEM FORMULATION 77
B DERIVATION OF SENSITIVITY MATRIX 80
B.0.1 EEG 80
B.0.2 MEG 81

LIST OF TABLES

TABLES

Table 3.1 FEM meshes with different number of nodes, elements and element types. 14

Table 3.2 The initially assigned conductivity values for brain, CSF, skull, scalp. 30

Table 3.3 The initially assigned conductivity values increased by 0.1%, 1% and 10%. 32

Table 3.4 The calculated conductivity values. Potential difference obtained from 221 electrodes are used. 32

Table 3.5 The calculated conductivity values. Potential difference obtained from 221 electrodes are used. A gaussian noise with a standard deviation of 10% of maximum measurement is added to the measurements. 32

Table 3.6 The calculated conductivity values. Magnetic fields difference obtained from 221 sensors are used. 33

Table 3.7 The calculated conductivity values. Magnetic fields difference obtained from 221 number of sensors are used. A gaussian noise with a standard deviation of 10% of maximum measurement is added to the measurements. 33

Table 3.8 The computed RDM values. Potential difference obtained from 221 electrodes are used. 34

Table 3.9 The computed RDM values. Potential difference obtained from 221 electrodes are used. A gaussian noise with a standard deviation of 10% of maximum measurement is added to the measurements. 34

Table 3.10 The computed RDM values. Magnetic fields difference obtained from 221 sensors are used. 34

Table 3.11 The computed RDM values. Magnetic fields difference obtained from 221 number of sensors are used. A gaussian noise with a standard deviation of 10% of maximum measurement is added to the measurements. 34

Table 3.12 The initially assigned conductivity values for brain, CSF, skull, scalp, fat, eye. 50

Table 3.13 The initially assigned conductivity values increased by 0.1%, 1% and 10%. 51

Table 3.14 The calculated conductivity values. Potential difference obtained from 25 electrodes are used. 51

Table 3.15 The calculated conductivity values. Potential difference obtained from 221 electrodes are used. A gaussian noise with a standard deviation of 10% of maximum measurement is added to the measurements. 51

Table 3.16 The calculated conductivity values. Magnetic fields difference obtained from 25 sensors are used. 51

Table 3.17 The calculated conductivity values. Magnetic fields difference obtained from 25 sensors are used. A gaussian noise with a standard deviation of 10% of maximum measurement is added to the measurements. 51

Table 3.18 The computed RDM values. Potential difference obtained from 25 electrodes are used. 52

Table 3.19 The computed RDM values. Potential difference obtained from 25 electrodes are used. A gaussian noise with a standard deviation of 10% of maximum measurement is added to the measurements. 52

Table 3.20 The computed RDM values. Magnetic fields difference obtained from 25 sensors are used. 53

Table 3.21 The computed RDM values. Magnetic fields difference obtained from 221 sensors are used. A gaussian noise with a standard deviation of 10% of maximum measurement is added to the measurements. 53

LIST OF FIGURES

FIGURES

Figure 2.1 The necessary steps for calculating the actual conductivity distribution of a given head. 12

Figure 2.2 The necessary steps for calculating the conductivity distribution of head in a simulation study. 13

Figure 3.1 The cross section of a spherical FEM mesh. 15

Figure 3.2 Distribution of 221 potential sensor positions on a homogenous sphere. 15

Figure 3.3 Positions of 38 x-oriented unit dipoles on the cross section of spherical FEM mesh. 16

Figure 3.4 Positions of a single unit dipole on the cross section of spherical FEM mesh. 18

Figure 3.5 Actual conductivity distribution of head with an inhomogeneity inside (white region). 18

Figure 3.6 Reconstructed conductivity distribution of head with inhomogeneity inside (white region) for 38 dipoles. 19

Figure 3.7 Reconstructed conductivity distribution of head with inhomogeneity inside (white region) for a single dipole. 19

Figure 3.8 Realistic conductivity distribution of head with inhomogeneity inside (white region). 20

Figure 3.9 Reconstructed conductivity distribution of head when the conductivity of the inhomogeneity is 0.33033 S/m. 21

Figure 3.10 Reconstructed conductivity distribution of head when the conductivity of the inhomogeneity is 0.33033 S/m. A gaussian noise with a standard deviation of 10% of maximum measurement is added to the measurements. 21

Figure 3.11 Reconstructed conductivity distribution of head when the conductivity of the inhomogeneity is 0.363 S/m. 22

Figure 3.12 Reconstructed conductivity distribution of head when the conductivity of the inhomogeneity is 0.363 S/m. A gaussian noise with a standard deviation of 10% of maximum measurement is added to the measurements. 22

Figure 3.13 Reconstructed conductivity distribution of head when the conductivity of the inhomogeneity is 0.633 S/m. 23

Figure 3.14 Reconstructed conductivity distribution of head when the conductivity of the inhomogeneity is 0.633 S/m. A gaussian noise with a standard deviation of 10% of maximum measurement is added to the measurements. 23

Figure 3.15 The cross section of spherical FEM mesh and positions of 10 dipole sets, each having 3 dipoles oriented in x, y, z directions. 24

Figure 3.16 x cross section view of the head model. The top left view is conductivity distribution of head with inhomogeneity inside, top right view is the updated conductivity distribution of head with inhomogeneity inside for x oriented dipole, bottom left view is the updated conductivity distribution of head with inhomogeneity inside for y oriented dipole, bottom right view is the updated conductivity distribution of head with inhomogeneity inside for z oriented dipole. 25

Figure 3.17 z cross section view of the head model. The top left view is conductivity distribution of head with inhomogeneity inside, top right view is the updated conductivity distribution of head with inhomogeneity inside for x oriented dipole, bottom left view is the updated conductivity distribution of head with inhomogeneity inside for y oriented dipole, bottom right view is the updated conductivity distribution of head with inhomogeneity inside for z oriented dipole. 26

Figure 3.18 y cross section view of the head model. The top left view is conductivity distribution of head with inhomogeneity inside, top right view is the updated conductivity distribution of head with inhomogeneity inside for x oriented dipole, bottom left view is the updated conductivity distribution of head with inhomogeneity inside for y oriented dipole, bottom right view is the updated conductivity distribution of head with inhomogeneity inside for z oriented dipole. 27

Figure 3.19 The cross section of spherical FEM mesh structure and position of one dipole with 8 different orientation. 28

Figure 3.20 Reconstructed conductivity distribution of head with inhomogeneity inside with a conductivity of 0.363 S/m. 29

Figure 3.21 The cross section of spherical FEM mesh cross section and positions of 32 -x-oriented dipoles. 29

Figure 3.22 Distribution of 221 sensor positions for EEG measurements on Concentric Sphere. 30

Figure 3.23 Distribution of 221 sensor positions for MEG measurements on Concentric Sphere. 31

Figure 3.24 Realistic conductivity distribution of head with inhomogeneity inside (white region). 36

Figure 3.25 Reconstructed conductivity distribution of head with a inhomogeneity inside. Potential difference obtained from 221 electrodes are used. . . . 36

Figure 3.26 Reconstructed conductivity distribution of head with a inhomogeneity inside. Potential difference obtained from 221 are used. A gaussian noise with a standard deviation of 1% of maximum measurement is added to the measurements. 37

Figure 3.27 Reconstructed conductivity distribution of head with a inhomogeneity inside. Magnetic fields difference obtained from 221 sensors are used. . 37

Figure 3.28 Reconstructed conductivity distribution of head with a inhomogeneity inside. Magnetic fields difference obtained from 221 sensors are used. A gaussian noise with a standard deviation of 1% of maximum measurement is added to the measurements. 38

Figure 3.29 Realistic conductivity distribution of head with inhomogeneity inside (white region). 38

Figure 3.30 Reconstructed conductivity distribution of head with a inhomogeneity inside. Potential difference obtained from 221 electrodes are used. . . . 39

Figure 3.31 Reconstructed conductivity distribution of head with a inhomogeneity inside. Potential difference obtained from 221 electrodes are used. A gaussian noise with a standard deviation of 1% of maximum measurement is added to the measurements. 39

Figure 3.32 Reconstructed conductivity distribution of head with a inhomogeneity inside. Magnetic fields difference obtained from 221 sensors are used. . 40

Figure 3.33 Reconstructed conductivity distribution of head with a inhomogeneity inside. Magnetic fields difference obtained from 221 sensors are used. A gaussian noise with a standard deviation of 1% of maximum measurement is added to the measurements. 40

Figure 3.34 Realistic conductivity distribution of head with inhomogeneity inside (white region). 41

Figure 3.35 Reconstructed conductivity distribution of head with a inhomogeneity inside. Potential difference obtained from 221 electrodes are used. . . . 41

Figure 3.36 Reconstructed conductivity distribution of head with a inhomogeneity inside. Potential difference obtained from 221 electrodes are used. A gaussian noise with a standard deviation of 1% of maximum measurement is added to the measurements. 42

Figure 3.37 Reconstructed conductivity distribution of head with a inhomogeneity inside. Magnetic fields difference obtained from 221 sensors are used. . 42

Figure 3.38 Reconstructed conductivity distribution of head with a inhomogeneity inside. Magnetic fields difference obtained from 221 sensors are used. A gaussian noise with a standard deviation of 1% of maximum measurement is added to the measurements. 43

Figure 3.39 Realistic conductivity distribution of head with inhomogeneity inside (white region). 43

Figure 3.40 Reconstructed conductivity distribution of head with a inhomogeneity inside. Potential difference obtained from 221 electrodes are used. . . . 44

Figure 3.41 Reconstructed conductivity distribution of head with a inhomogeneity inside. Potential difference obtained from 221 electrodes are used. A gaussian noise with a standard deviation of 1% of maximum measurement is added to the measurements. 44

Figure 3.42 Reconstructed conductivity distribution of head with a inhomogeneity inside. Magnetic fields difference obtained from 221 sensors are used. . 45

Figure 3.43 Reconstructed conductivity distribution of head with a inhomogeneity inside. Magnetic fields difference obtained from 221 number of sensors are used. A gaussian noise with a standard deviation of 1% of maximum measurement is added to the measurements. 45

Figure 3.44 Realistic conductivity distribution of head with inhomogeneity inside (white region). 46

Figure 3.45 Reconstructed conductivity distribution of head with a inhomogeneity inside. Potential difference obtained from 221 electrodes are used. . . . 46

Figure 3.46 Reconstructed conductivity distribution of head with a inhomogeneity inside. Potential difference obtained from 221 electrodes are used. A gaussian noise with a standard deviation of 1% of maximum measurement is added to the measurements. 47

Figure 3.47 Reconstructed conductivity distribution of head with a inhomogeneity inside. Magnetic fields difference obtained from 221 sensors are used. . 47

Figure 3.48 Reconstructed conductivity distribution of head with a inhomogeneity inside. Magnetic fields difference obtained from 221 sensors are used. A gaussian noise with a standard deviation of 1% of maximum measurement is added to the measurements. 48

Figure 3.49 Realistic FEM mesh structure are composed of rectangular grids. . 48

Figure 3.50 Location of 14 dipole sets, each having 3 dipoles at the same location, 25 potential and magnetic sensors on the realistic head model. 49

Figure 3.51 Realistic conductivity distribution of head with inhomogeneity inside (white region). 54

Figure 3.52 Reconstructed conductivity distribution of head with a inhomogeneity inside. Potential difference obtained from 25 electrodes are used. 55

Figure 3.53 Reconstructed conductivity distribution of head with a inhomogeneity inside. Potential difference obtained from 25 electrodes are used. A gaussian noise with a standard deviation of 1% of maximum measurement is added to the measurements. 55

Figure 3.54 Reconstructed conductivity distribution of head with a inhomogeneity inside. Magnetic fields difference obtained from 25 sensors are used. . . 56

Figure 3.55 Reconstructed conductivity distribution of head with a inhomogeneity inside. Magnetic fields difference obtained from 25 sensors are used. A gaussian noise with a standard deviation of 1% of maximum measurement is added to the measurements. 56

Figure 3.56 Realistic conductivity distribution of head with inhomogeneity inside (white region). 57

Figure 3.57 Reconstructed conductivity distribution of head with a inhomogeneity inside. Potential difference obtained from 25 electrodes are used. 57

Figure 3.58 Reconstructed conductivity distribution of head with a inhomogeneity inside. Potential difference obtained from 25 electrodes are used. A gaussian noise with a standard deviation of 1% of maximum measurement is added to the measurements. 58

Figure 3.59 Reconstructed conductivity distribution of head with a inhomogeneity inside. Magnetic fields difference obtained from 25 sensors are used. . . 58

Figure 3.60 Reconstructed conductivity distribution of head with a inhomogeneity inside. Magnetic fields difference obtained from 25 sensors are used. A gaussian noise with a standard deviation of 1% of maximum measurement is added to the measurements. 59

Figure 3.61 Realistic conductivity distribution of head with inhomogeneity inside (white region). 59

Figure 3.62 Reconstructed conductivity distribution of head with a inhomogeneity inside. Potential difference obtained from 25 electrodes are used. 60

Figure 3.63 Reconstructed conductivity distribution of head with a inhomogeneity inside. Potential difference obtained from 25 electrodes are used. A gaussian noise with a standard deviation of 1% of maximum measurement is added to the measurements. 60

Figure 3.64 Reconstructed conductivity distribution of head with a inhomogeneity inside. Magnetic fields difference obtained from 25 sensors are used. . . 61

Figure 3.65 Reconstructed conductivity distribution of head with a inhomogeneity inside. Magnetic fields difference obtained from 25 sensors are used. A gaussian noise with a standard deviation of 1% of maximum measurement is added to the measurements. 61

Figure 3.66 Realistic conductivity distribution of head with inhomogeneity inside (white region). 62

Figure 3.67 Reconstructed conductivity distribution of head with a inhomogeneity inside. Potential difference obtained from 25 electrodes are used. 62

Figure 3.68 Reconstructed conductivity distribution of head with a inhomogeneity inside. Potential difference obtained from 25 electrodes are used. A gaussian noise with a standard deviation of 1% of maximum measurement is added to the measurements. 63

Figure 3.69 Reconstructed conductivity distribution of head with a inhomogeneity inside. Magnetic fields difference obtained from 25 sensors are used. . . 63

Figure 3.70 Reconstructed conductivity distribution of head with a inhomogeneity inside. Magnetic fields difference obtained from 25 sensors are used. A gaussian noise with a standard deviation of 1% of maximum measurement is added to the measurements. 64

Figure 3.71 Realistic conductivity distribution of head with inhomogeneity inside (white region). 64

Figure 3.72 Reconstructed conductivity distribution of head with a inhomogeneity inside. Potential difference obtained from 25 electrodes are used. 65

Figure 3.73 Reconstructed conductivity distribution of head with a inhomogeneity inside. Potential difference obtained from 25 electrodes are used. A gaussian noise with a standard deviation of 1% of maximum measurement is added to the measurements. 65

Figure 3.74 Reconstructed conductivity distribution of head with a inhomogeneity inside. Magnetic fields difference obtained from 25 sensors are used. . . 66

Figure 3.75 Reconstructed conductivity distribution of head with a inhomogeneity inside. Magnetic fields difference obtained from 25 sensors are used. A gaussian noise with a standard deviation of 1% of maximum measurement is added to the measurements. 66

CHAPTER 1

INTRODUCTION

1.1 General Overview

Internal body functions or an external stimulus create electric sources in the human brain. These sources generate electric potentials on the head surface and magnetic fields nearby the head. Electric potentials can be monitored by electrodes attached on the head surface (Electroencephalography-EEG) and magnetic fields are monitored by magnetic sensors over the scalp (Magnetoencephalography-MEG). Sources in the brain can be modeled as electric dipoles, and location, orientation and strength of these dipoles are displayed by Electro-magnetic Source Imaging (EMSI) [1] [2]. The forward problem of EMSI is the calculation of the potential distribution on the head surface and magnetic fields nearby the head for a given head model and source configuration. The inverse problem algorithm uses the calculated fields and measurements to obtain the unknown source configuration. For the forward problem solutions, human head can be modelled by concentric spheres. Analytical solutions are available for the spherical models, however numerical methods are necessary for realistic models. Thus, Boundary Element Method (BEM), Finite Difference Method (FDM) and Finite Element Method (FEM) are usually employed to develop realistic models. The BEM solves the potential and magnetic fields on the boundary of different tissues, and can not handle conductivity anisotropy. The FDM handles the conductivity anisotropy by assigning different conductivity value to each element used in the model. A better solution is to use the FEM which allows conductivity anisotropy, and triangular and quadratic elements in modeling. However, mesh generation for a mesh with quadratic elements is quite a difficult problem. Success in determining the location of the activity in EMSI depends on the digital head model that is used to represent the human head and the realistic conductivity distribution. For the forward problem calculations, mean conductivity values that are available in the literature are assigned for tissues used in the head model. However, this approach might lead to incorrect source localization problems [3] [4] [5] [6] [7] [8] [9] [10] [11], and perturbations in the conductivity distribution affect both EEG and MEG measurements [3] [12] [13] [14] [15] [16]. Mean conductivity values may change from individual to individual. For a given head, the conductivity of a specific tissue may also vary as a function of position [17]. Consequently, the actual conductivity distribution must be determined [18]. This thesis study presents a novel approach to obtain conductivity of head tissues using evoked fields and potentials.

Various methods have been introduced for imaging conductivity distribution of the human head. However, none of these methods have used evoked fields and potentials for this estimation. This thesis study is based on the sensitivity matrix approach developed to find the sensitivity of EEG and MEG measurements to tissue conductivity perturbations [12]. In that study, Gençer and Acar computed sensitivity matrix using a FEM based approach, and noted that this approach can be used for computing the conductivity distribution of the human head.

For the forward problem computations, calculation of the sensitivity matrix and in the solution of linear system of equations, a high-performance computing environment is required. Thus, in previous studies a paralel PC cluster of 8 computers was designed and developed [19] [20]. Portable, Extensible Toolkit for Scientific Computation (PETSc) library was chosen for parallel system solver.

1.2 Objective of the Study

The aims of this thesis study are:

- To calculate the sensitivity matrix that relates the EEG and MEG measurements to conductivity perturbations.
- To solve a large-scale, ill-posed linear system of equation using least-squares QR

(LSQR) algorithm of PETSc.

- To calculate the conductivity values of tissues.
- To reconstruct the conductivity distribution of human head using FEM based sensitivity approach.
- To image the inhomogeneities in human head.

1.3 Significance of the Study

In EMSI, mean conductivity values are used for each tissue in the human head. This leads to source localization problems. Besides, conductivity perturbations (i.e, inhomogeneities) disturb the EEG and MEG amplitudes. Thus, a means to monitor the conductivity distribution of a human head is required. This study proposes a novel approach to determine the actual conductivity distribution of the human head from evoked fields and potentials.

1.4 Outline of the Thesis

This thesis study consists of four chapters. The first chapter provides a general overview, and presents objective and significance of this study. The next chapter presents a summary of the relavant literature and discusses the importance of conductivity imaging. The second chapter also provides the theoretical background behind the proposed approach. Chapter 3 provides the result of the simulation studies that validate the theoretical knowledge. Conclusions and discussions are presented in the last chapter.

CHAPTER 2

IMAGING THE CONDUCTIVITY DISTRIBUTION OF THE HUMAN HEAD

2.1 Introduction

Specific regions within the human brain are responsible for controlling various body functions. Moreover, mental [21] or neurological and neuropsychological disorders such as epilepsy [22], depression, schizophrenia, Parkinson's and Alzheimer's diseases [1] can be due to the abnormal functions of specific regions (or due to a possible physical damage occuring at these regions). Thus, finding the origin of these abnormal functions is one of the most interesting topic of the brain research. This requirement leads to the development of many brain imaging modalities. Positron Emission Tomography (PET), Single Photon Emission Computed Tomography (SPECT) and Magnetic Resonance Imaging (MRI) [23] are the modalities used for brain imaging and mapping purposes. Spatial information provided by these techniques are sufficient, however they suffer from the temporal resolution. For instance, the spatial resolution of PET is 2 mm, however temporal resolution can be several minutes [1]. Lack of an accurate temporal information is an important problem in understanding the realistic behaviour of human brain under external stimuli such as auditory or visual stimuli or the internal processes of the brain, such as thinking. Thus, Electroencephalography (EEG) and Magnetoencephalography (MEG), which have temporal resolution below 100 ms [1], are introduced as new measurement methods for brain mapping. However, the spatial resolution of both EEG and MEG is not accurate as PET, SPECT, MR and needs to be improved.

EEG measures the electric field by electrodes attached on the scalp surface. MEG measures magnetic fields by magnetic sensors called super-conducting quantum interference devices (SQUID) over the head [24]. These electrical and magnetic fields are due to the activity of the specific regions of the brain. These regions are electrically active and are the sources of both electric and magnetic fields. The electrical activities can be assumed source points and is usually modeled by electrical dipoles. Electromagnetic source imaging (EMSI) is used for determining the position, orientation and strength of these dipoles. For this purpose, the human head is modeled numerically, and potentials and magnetic fields are solved for a known dipole configuration (forward problem). Comparing the forward problem solutions with the measured electric and magnetic fields, the position, orientation and strength of the dipole can be estimated (inverse problem). The word "estimation" in the previous sentence is used purposely, since finding the position, orientation and strength of dipole depends on a number of factors, such as, the head model used in the calculation, sensor positions, the algorithm used for the solution of the corresponding inverse problem, etc.

Homogenous sphere, concentric sphere with three or four layers or eccentric sphere head models lead to significant errors in source localization [12]. To minimize the errors more realistic head models are used. In order to fulfill this requirement, the digital head models are formed from MR images by using segmentation algorithms and the geometric models of different tissues are obtained [25].

Success in determining the location of the activity in EMSI depends on the geometry of the head model, and the realistic conductivity distribution. Usually, the mean conductivity values are assigned for the tissues used in the head model. However, this approach might lead to incorrect source localization problems, since mean conductivity may change for different individuals. The conductivity of a specific tissue (for example, skull) may change as a function of position [17]. Thus, there is a need to update the assigned conductivity values and refine the model [18].

In the literature, there are several studies that have investigated the effect of volume conduction behaviour of human brain on source localization and on amplitudes of both EEG and MEG measurements. A review of these studies is given below:

- Simulaton studies showed that, anisotropic volume conduction in the brain affects both source localization and amplitudes of EEG and MEG [3].

- Cuffin investigated the effect of a bubble in the brain on the measurements and stated that a bubble affects the amplitudes of the masurements [13].
- Schnedeir investigated the scalp and skull inhomogeneties and reported a failure in finding the dipole strength and location [4].
- In 1982, Cuffin investigated the effects of inhomogeneous regions on the field measurements. It is reported that, if conductivity of the inhomogeneous region is less than the conductivity of the entire volume then this decreases the potential fields and perpendicular magnetic fields [14].
- Benar investigated the post-surgical brain and skull defects in the EEG inverse problem and stated that there are errors in source estimation due to these defects [5].
- The perturbations in the vicinity of the source affects both the MEG and EEG signals (EEG and MEG is sensitive to the perturbations close to the source), moreover EEG is also sensitivite to the changes in the conductivity of tissues near the electrodes [15].
- For a four-layer sphere model of head, it was shown that 20% changes in the layer conductivities lead to over 60% changes in the potential values [16].
- Bill and Kevin investigated the effect of model uncertainty problems on source localization using EEG measurements and concluded that changes in the conductivity affects the source localization more than radii does [6]. They used a four-layer sphere model.
- The holes in the skull result in large effects on EEG measurements whereas it has negligible effect on MEG (anisotropy in skull have smeering effect on EEG but no effect on MEG). It was also reported that, a lesion changes both EEG and MEG measurements and it must be taken into account when it is close to the source [7].
- Simulation studies show that overestimation or underestimation of the actual skull conductivity value leads to dipole localization errors when realistic head models are used with EEG [8].

- Neglecting holes in the skull and the effect of ventricular system and underestimating the skull conductivity in EEG leads to localization errors [9].

- MEG and EEG are affected strongly by the inhomogeneities in the vicinity of the source [26]. If active area is modeled by more than one dipole (multiple sources), then a more realistic head model is required [27]. Moreover, Akalın investigated the effect of eye tissue conductivity on the forward problem by using Boundary Element Method (BEM) and stated that if the dipole is close to the eye the Relative Difference Measure (RDM) increases [27].

- The effect of conductivity anisotropy was investigated on source localization for Early Left Anterior Negativity (ELAN) component in the language processing, and it is stated that the for EEG the conductiviy anisptropy deeply affects the source localization procedure, however for MEG it has no deep effect [10].

- Accuracy in estimating the location, distribution and intensity of brain activity is highly dependent on the conductivity distribution of the head [11].

In short, the realistic conductivity distribution of the human head is required for more accurate source localization. Thus, various medical imaging techniques are proposed for monitoring the tissue conductivity up to now. In applied-current electrical impedance tomography (ACEIT), the current is applied to an individual via electrodes that are attached to the surface, and as a response to the applied current, the voltages are measured by different electrode pairs [28] [29]. By changing the current drive pair, it is possible to increase the number of measurements. Thereafter, mathematical algorithms are employed to monitor the conductivity values of tissues. In induced-current electrical impedance tomography (ICEIT), the sole purpose of the electrodes is to measure the voltage [30] [31] [32]. Current is induced to body via time varying magnetic fields. In the recent years, a new contactless technique is also proposed as a new imaging modality. In this technique, current is induced and magnetic fields are measured without using any electrodes [33] [34] [35] [36] [37] [38] [39] [40]. The number of researches on developing hybrid techniques, such as combining magnetic resonance imaging (MRI) with applied current and/or induced current (EIT), are increasing in the recent years [41] [42] [43] [44].

Up to now, finding the electrical conductivity distribution of human head by using evoked fields and potentials has not been investigated in detail. In 1987, Nunez proposed a method to estimate the local skull resistance by using the known brain activity and surface measurements [45], however, no simulation or experimental results were given. Baysal and Haueisen, also, used the evoked responses recorded by applying somato-sensory stimulus to estimate the resistivities of scalp, skull and brain [46]. The authors employed a statistically constrained minimum mean squared error estimator (MIMSEE) to estimate the resistivity values. In 2004, Acar and Gençer derived two formulations that relate the sensitivity of EEG and MEG measurements to tissue conductivity [12]. In that study, they proposed that this approach can be used to compute the realistic conductivity distribution of the human head, but they did not provide any experimental or simulation results. The next section gives the definition and formulation of that approach.

2.2 Sensitivity of EEG and MEG measurements to tissue conductivities

In the previous section, the methods for monitoring the realistic conductivity distribution of human head are reviewed. The aim of this section is to present the mathematical formulation required to update the initially assigned conductivity distribution. This formulation was reported in detail in [12]. In that study the authors investigated the sensitivity of EEG and MEG measurements to tissue conductivities using the FEM based sensitivity matrix approach. The authors focused on the following goals:

- determining the regions where the EEG and MEG measurements are more sensitive,
- determining the tissue type(s) that affects the measurements,
- comparison of the EEG and MEG measurements under conductivity perturbations,

Gençer and Acar concluded that this approach can also be used to update the initially assigned conductivity values and proposed the use of the following two equations [12]:

$$\Delta\Phi_s = S_\Phi \Delta\sigma \tag{2.1}$$

$$\Delta B = S_B \Delta\sigma \tag{2.2}$$

where S_Φ and S_B denote the sensitivity matrices for voltage and magnetic field measurements, $\Delta\Phi_s$ is the voltage change in the electrode positions, ΔB is the magnetic field change in the magnetic sensors, and $\Delta\sigma$ is the change in the conductivities. Sensitivity matrix is the coefficient matrix that relates the change in the conductivity with the change in the measurements. The dimension of sensitivity matrix depends on number of sensors and number of elements used in FEM mesh.

The sensitivity matrix can be evaluated for each element in the model by solving the forward problem twice. For the first solution, the mean conductivity distribution is used. In the second case, the conductivity of a single element is changed (for example, by %1) and forward problem is solved again. This procedure can be repeated for each element in the head and each entry of the sensitivity matrix can be calculated. However, solving the forward problem for each element is time consuming and computationally very expensive. Thus, instead of using this approach, computationally more efficient method was developed [12]. Appendix B gives brief description of this approach to calculate the sensitivity matrix.

Forward problem of EMSI and linear system of equations are solved in a parallel computing environment named ATHLIN. ATHLIN was developed by Yoldaş Ataseven [20]. This paralel computing environment is composed of 8 PCs (nodes) each having AMD Athlon XP 1.83 GHz processor and 1.5GHz RAM. Nodes are communicating with each other via LAN (Beowulf cluster). Besides, an extra PC, named MARVIN, is assigned to control this computation platform. The operating system for ATHLINs is Linux and for MARVIN is FreeBSD. To develop and use this workstation as a paralel cluster several libraries (both sicentific ve message passing) needs to be installed. Message Passing Interface (MPI) is used for inter-process commmunication and Portable, Extensible Toolkit for Scientific Computation (PETSc) is used for linear solver. PETSc is composed of data structures and routines that are used to solve the linear system of equations. And, PETSc provides opportunity to use both direct and iterative techniques. However its great strentgh lies on the iterative solutions for the sparse matrices. Besides PETSc allows to solve dense matrices. PETSc, by using MPI routines implicitly, provides a high level interface for distributing the large scale matrices over the nodes [47] [48] [49]. Distributing matrices have two advantages. One is the decrease in the computation time, and the other is increase in RAM size. Thus, larger matrices can be handled and computed in a lesser time.

The conductivity computation requires the solution of either Equation (2.1) or Equation (2.2). The direct and iterative methods are used for the solution of linear system of equations. Direct methods are applied to the linear system whenever there exists a unique solution. To find a unique solution, the sensitivity matrix should be square and have full rank. Besides, the dimension of sensitivity matrix is high and solving such kind of large scale linear systems using direct methods is a time consuming problem .Thus, direct methods are not applicable for our case. However, iterative methods can be applied. Moreover, they are useful for the linear systems that do not have single solution. The iterative methods start with an initial guess and make iterations until the norm of an error vector gets smaller (least square solution). By doing so, the optimum solution can be chosen among all possible solutions.

Krylov Subspace Methods (KSM), like the biconjugate gradient (bicg), Biconjugate gradient stabilized (bicgstab), Conjugate gradient squared (cgs), Generalized minimum residual (gmres), Least Square QR (lsqr), Minimum residual (minres), Preconditioned conjugate gradient (pcg), Quasiminimal residual (qmr), Symmetric LQ (symmlq), are well known iterative methods for linear equations [50]. KSM generates a sequence of orthogonal basis vectors. These basis vectors form a subspace, and approximate solutions are found minimizing the residuals on this subspace [50]. Thus, parallel solver for Equations (2.1) and (2.2) is developed using PETSc library which allow to use KSM.

As stated earlier, sensitivity matrix is ill-conditioned. Thus, truncated singular value decomposition and tikhonov regularization methods may be requiered. However, such direct methods are not practical since sensitivity matrix is large [51]. The alternative may be to use the iterative Krylov subspace methods for regularization purposes [51]. Krylov subspace methods project of coefficient matrix into a smaller subspace [52]

[53] [54] [51] and approximate solutions can be found in an iterative manner [52]. The least square QR (LSQR) method is one of the Krylov subspace methods and is based on Golub and Kahan bidiagonalization [55] and QR factoriazation. LSQR generates a sequence of approximations and decreases the residiual norm [56]. This sequence is equivalent to the subspaces created by Krylov Subspace methods. LSQR approaches the optimal regularization solution after a few iterations and if the iterations are not stopped the method may converge to a worse solution with high relative error [51]. Thus, regularization for ill-conditioned matrices can be achieved by early termination of iterations [57]. By terminating the iterations at k steps, the solution is projected onto a k-dimesional subspace, and this has the regularizing effect [52].

2.3 Procedure

The aim of this section is to present the necessary steps for calculating the conductivity distribution (shown in Figure 2.1). Conductivity calculations start with the solution of the EMSI forward problem. It is assumed that an auditory, visual or a somato-sensory stimulus is applied to the patient. As a response to this stimulus time varying electrical activities are to be generated within the brain. The location of these activities will be estimated by solving the inverse problem of EMSI for a specified head model. After obtaining the number and locations of dipoles, sensitivity matrix for each dipole is computed. The next step is to solve the Equation (2.1) for EEG measurements and Equation (2.2) for MEG measurements. This will give the difference between the realistic and initially assigned conductivity distribution. If the procedure is repated, based on the dipole and conductivity configuration obtained in the previous step, it may be possible to obtain more realistic dipole and conductivity distribution.

Finding a more accurate source configuration is a possible application of this approach, however it is out of scope of this thesis study and will be offered as a future work. The performance in calculating the conductivity distribution is the main purpose of this study. Thus, we assume that the source dipole configuration is already determined. For a known dipole locations and initially assigned conductivity values, the forward problem will be solved. In summary, in the simulation studies the following will be applied :

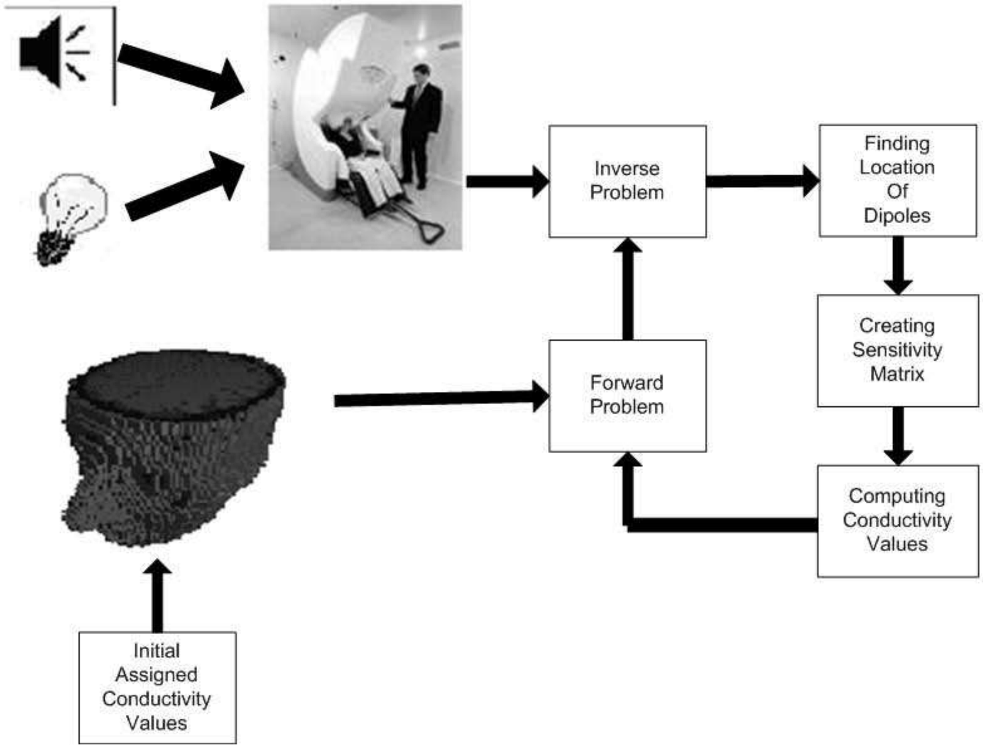

Figure 2.1: The necessary steps for calculating the actual conductivity distribution of a given head.

- a numerical head model is developed,
- location, orientation and strength of dipoles are specified,
- the number and locations of the electrodes and magnetic sensors are specified,
- initial conductivity is assigned for each element in the model,
- the potential and magnetic field distribution is calculated (forward problem, see Appendix A for forward problem procedure),
- the sensitivity matrix for each dipole is created (see Appendix B for sensitivity matrix calculation),
- for the same head model with the same sensor and dipole configuration change the initially assigned conductivity distribution (it can be specific location in the model or the whole tissue conductivity value can be changed) and solve the potential and magnetic field distribution again,

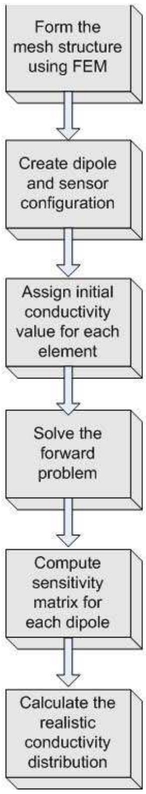

Figure 2.2: The necessary steps for calculating the conductivity distribution of head in a simulation study.

- take the difference between two measurements. These are the differences in the potential and magnetic measurements, put this vector to the left hand side of Equation (2.1) for potential measurements and Equation (2.2) for magnetic field measurements,

- put the sensitivity matrix in the right hand side of the Equation (2.1) for potential measurements and Equation (2.2) for magnetic field measurements and solve the linear system of equation,

- output of the linear system of equations gives the change in the conductivity distribution. The conductivity values can be updated by adding the initially assigned values with the solutions,

CHAPTER 3

RESULTS

3.1 Introduction

Equations described in the previous section are solved to investigate the accuracy of the adopted approach to calculate the conductivity distribution. For this purpose, the procedures described in Figure 2.2 are followed and simulation results are presented for head models in Table 3.1. First, the conductivity distribution of a homogenous sphere is computed. Then, the effects of the number of measurements on the condition number (via increasing the number of dipoles or varying orientation of a fixed single dipole) are investigated using the homogenous sphere. Next, the effects of contrast (between the inhomogeneity and brain) and dipole orientations on the imaging performance are presented. Last two sections are devoted to the tissue conductivity calculation and inhomogeneity imaging for concentric sphere and realistic head model.

Table 3.1: FEM meshes with different number of nodes, elements and element types.

	Type	Number of Nodes	Number of Elements
Homogeneous Sphere	Quadratic	31405	7600
Concentric Sphere	Quadratic	92861	22736
Realistic	Linear	118193	108514

3.2 Homogenous Sphere

In this section, a FEM mesh consisting of 31405 nodes and 7600 elements is used to represent a homogenous sphere (Figure 3.1) with an initially assigned conductivity value of 0.33 S/m. The voltages are measured using 221 electrodes attached on the head surface (Figure 3.2). An electrode at the occipital area is chosen as the reference electrode. Different dipole locations and orientations are used, therefore dipole configurations are presented in each experiment.

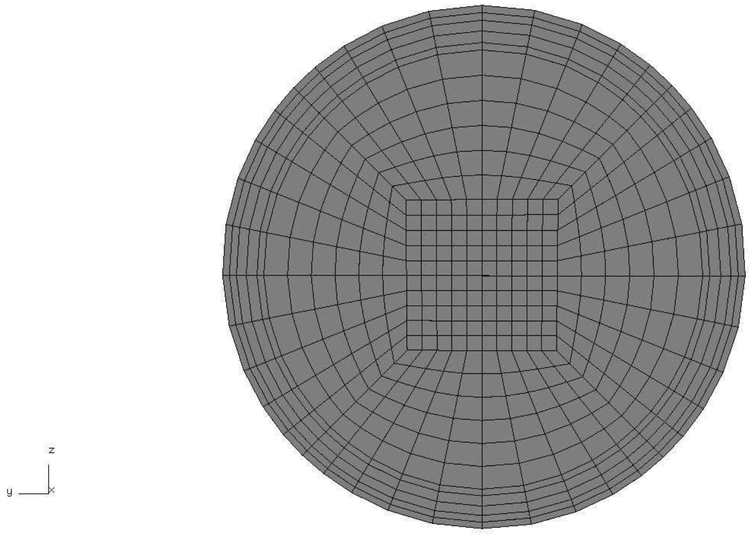

Figure 3.1: The cross section of a spherical FEM mesh.

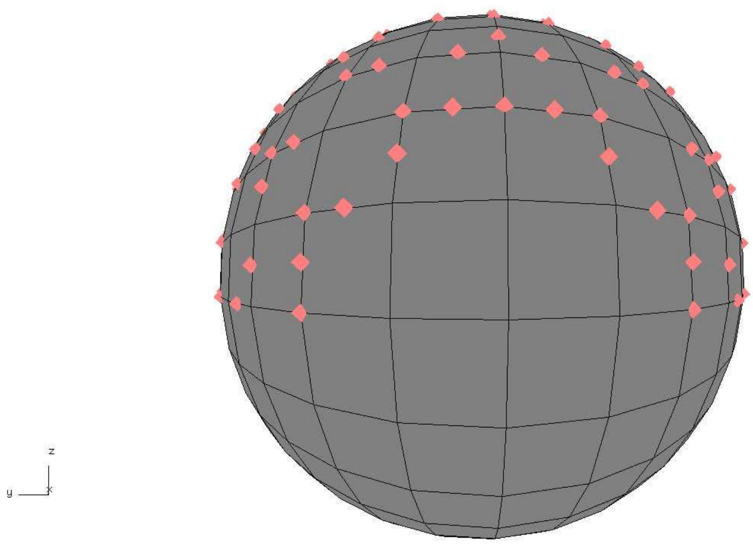

Figure 3.2: Distribution of 221 potantial sensor positions on a homogenous sphere.

3.2.1 Reconstructing the conductivity distribution of a homogeneous sphere

The objective of this section is to reconstruct the conductivity of the homogeneous sphere. Thus, conductivity of all elements in the head model are assumed to be uniform (0.33 S/m). Potential fields on 221 electrodes (Figure 3.2) are calculated by solving the forward problem for 38 dipoles (Figure 3.3). A gaussian noise with a standard deviation of 10% of maximum measurement is added to the measurements. Equation (2.1) is solved, and Relative Difference Measure (RDM), given by Equation (3.1), is used to compare the calculated and actual conductivity values. The RDM value is obtained as 0.0138% which shows the adopted method calculates the conductivity distribution accurately. The percentage RDM value is calculated based on the following formula:

$$\%RDM = \sqrt{\frac{\sum_{i=1}^{N}(x_i^r - x_i^u)^2}{\sum_{i=1}^{N}(x_i^r)^2}} \times 100 \tag{3.1}$$

where x_i^r represents the actual conductivity of the ith element, x_i^u represents the calculated conductivity value of the corresponding element, and N is the number of elements.

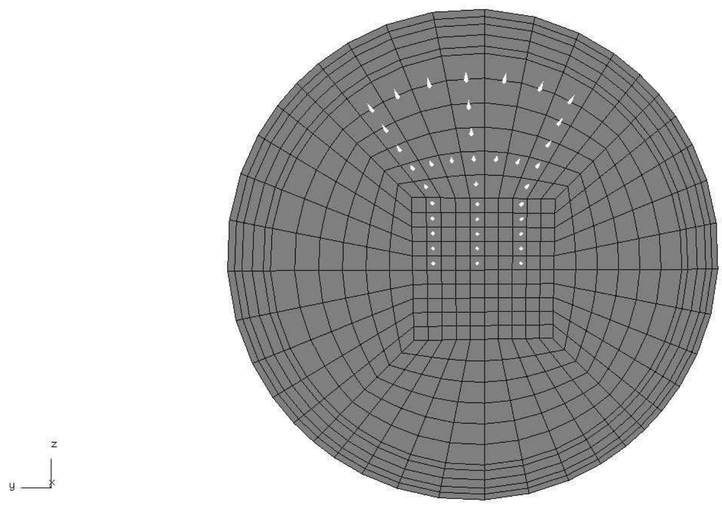

Figure 3.3: Positions of 38 x-oriented unit dipoles on the cross section of spherical FEM mesh.

3.2.2 Effects of the number of measurements on the condition number

Computing the conductivity distribution of a human head using Equation (2.1) is an ill-posed problem. As stated earlier, the size of the sensitivity matrix is determined by the number of sensors and number of elements in the FEM mesh. In the previous simulation study, the number of electrodes is assumed as 221. The head model is developed using 7600 elements. Thus, the sensitivity matrix is an 221×7600 matrix. The condition number (1.13e+20) shows that the sensitivity matrix is ill-conditioned. To increase the number of independent measurements the number of sources (dipoles) may be increased. If sensitivity matrices for each dipole are appended one after another, then for example, for 38 dipoles an 8398×7600 $((221 * 38) \times 7600)$ larger sensitivity matrix can be obtained. The condition number of that sensitivity matrix is 2.71e+12 which is quite large, but less than that obtained for a single dipole position. Normally, the sensitivity matrix with higher condition number should be less succesful in computing the conductivity distribution.

Figure 3.5 shows an inhomogeneity in an otherwise homogeneous head model. Starting from a homogeneous head model, our goal is to obtain the actual conductivity distribution of the head, i.e., to detect the inhomogeneity inside the head. The corresponding sensitivity matrix is calculated and is used to find a better estimate of the conductivity distribution. Figure 3.6 shows the reconstructed conductivity distribution when 38 dipoles (Figure 3.3) are used. The size and location of the inhomogeneity can be distinguished. Figure 3.7 shows the reconstructed distribution when a single dipole (Figure 3.4) is used. It is not possible to identify the inhomogeneity in the head. This study clearly shows that in order to reconstruct better conductivity images the number of sources (identified by ESI studies) should be increased.

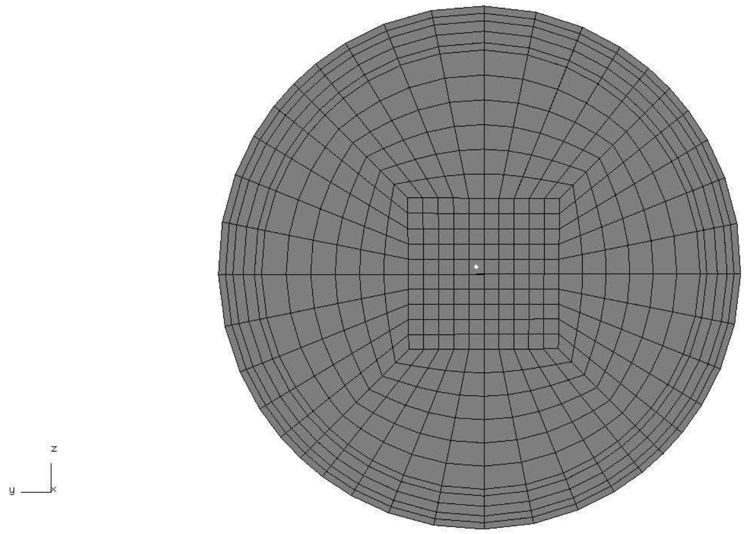

Figure 3.4: Positions of a single unit dipole on the cross section of spherical FEM mesh.

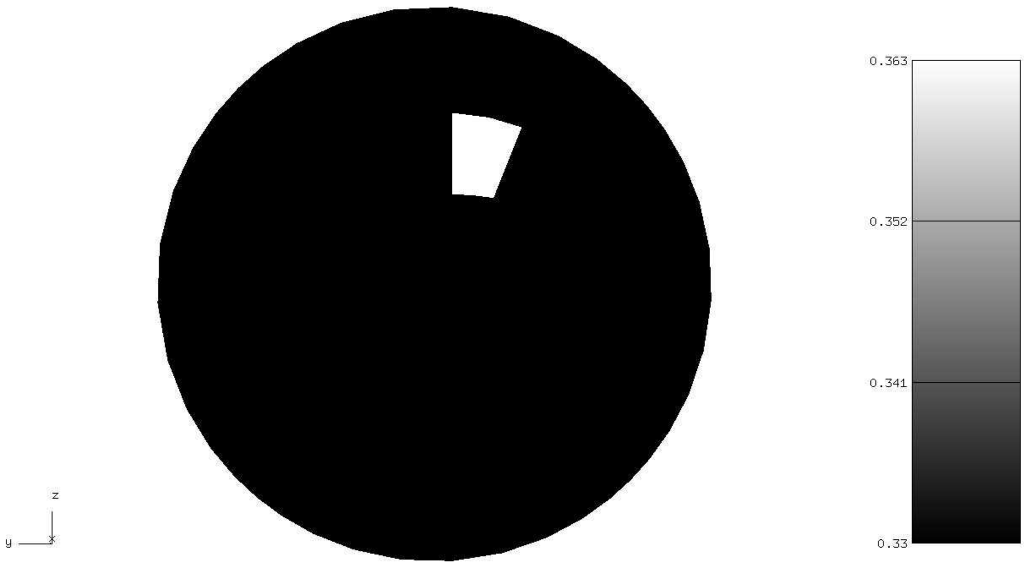

Figure 3.5: Actual conductivity distribution of head with an inhomogeneity inside (white region).

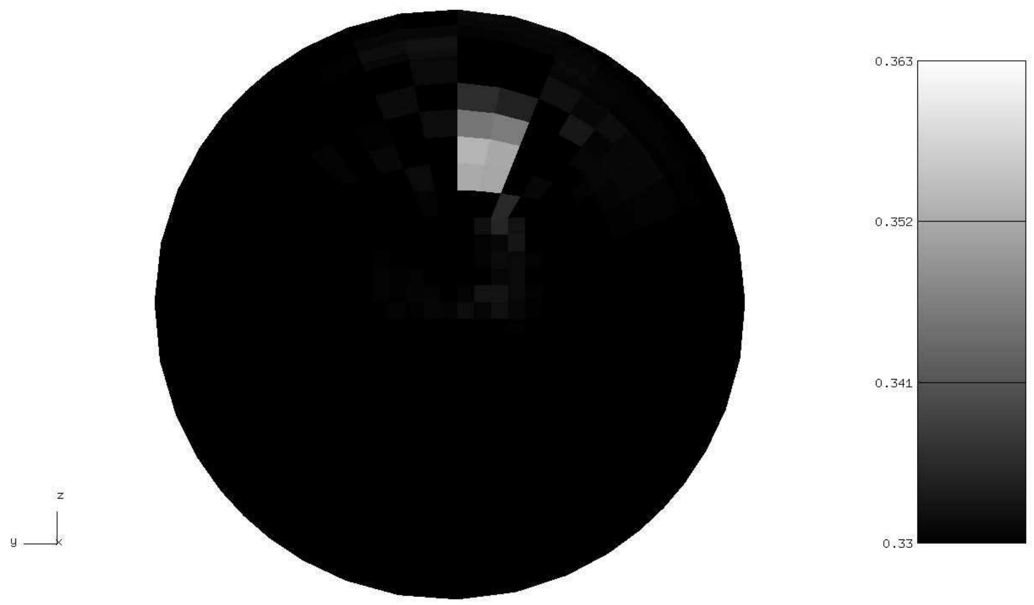

Figure 3.6: Reconstructed conductivity distribution of head with inhomogeneity inside (white region) for 38 dipoles.

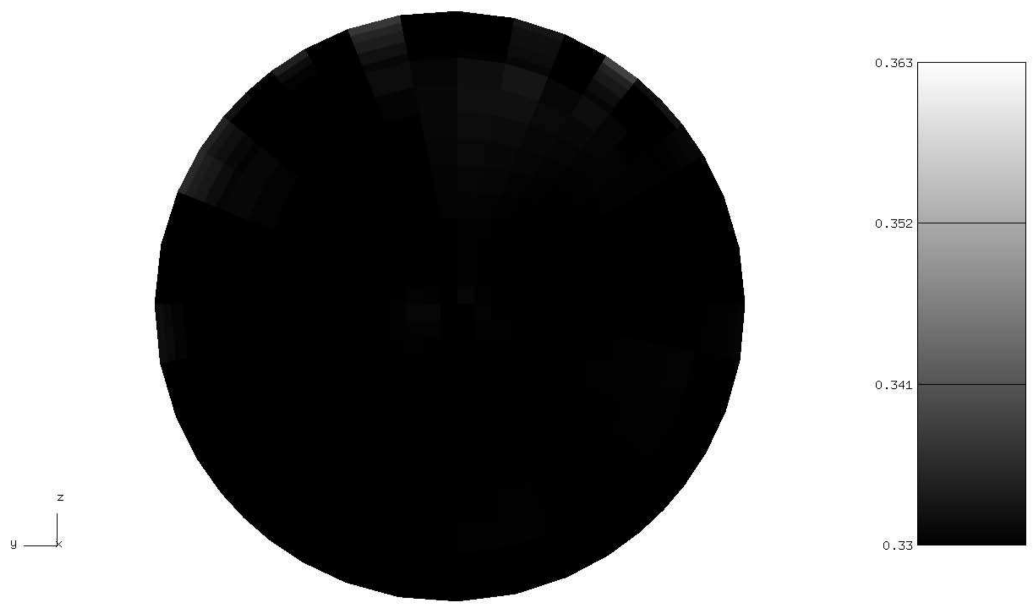

Figure 3.7: Reconstructed conductivity distribution of head with inhomogeneity inside (white region) for a single dipole.

3.2.3 Contrast Resolution

The topic of this section is to investigate the effects of contrast (between the inhomogeneity and brain) on the imaging performance. For this purpose, an inhomogeneity is assumed in the head, as shown in Figure 3.8. In three different head models, the conductivity of the inhomogeneity is changed. 0.33033 S/m, 0.363 S/m and 0.633 S/m are the assigned conductivity values of the inhomogeneity. The measurements are obtained from 221 electrodes and a gaussian noise with a standard deviation of 10% of maximum measurement is added to the measurements. Figures 3.9, 3.11, 3.13 show the reconstructed conductivity distribution of the inhomogeneity when the assigned conductivity values of the inhomogeneity are 0.33033 S/m, 0.363 S/m and 0.633 S/m. Figures 3.10, 3.12, 3.14 show the reconstructed conductivity distribution of the inhomogeneity when the assigned conductivity values of the inhomogeneity are 0.33033 S/m, 0.363 S/m, 0.633 S/m and when noise is added to the measurements. This study, for noisless measurements, shows that, the size and location of inhomogeneity can be distinguished for any conductivity value. However, when noise is added, increase in the conductivity of the inhomogeneity leads to better reconstruction of inhomogeneity.

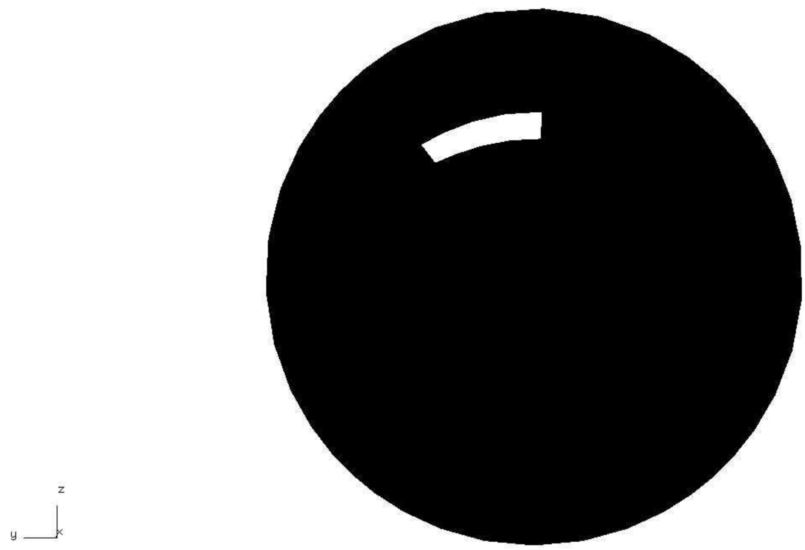

Figure 3.8: Realistic conductivity distribution of head with inhomogeneity inside (white region).

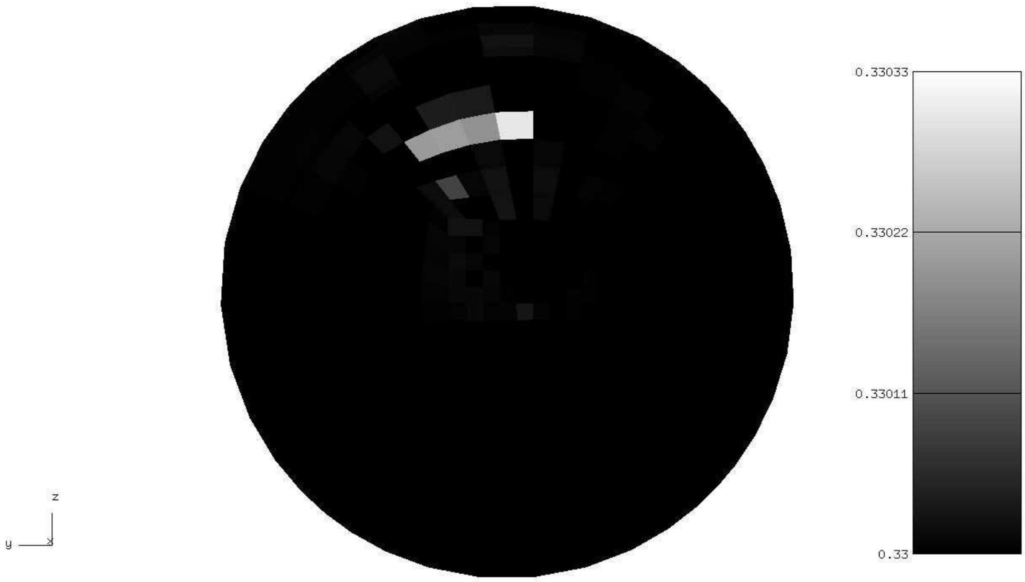

Figure 3.9: Reconstructed conductivity distribution of head when the conductivity of the inhomogeneity is 0.33033 S/m.

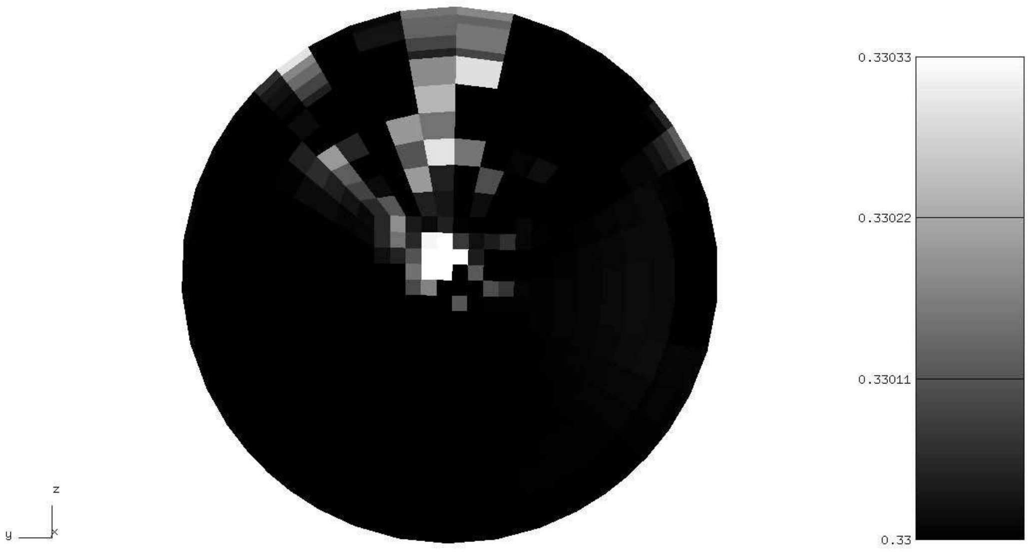

Figure 3.10: Reconstructed conductivity distribution of head when the conductivity of the inhomogeneity is 0.33033 S/m. A gaussian noise with a standard deviation of 10% of maximum measurement is added to the measurements.

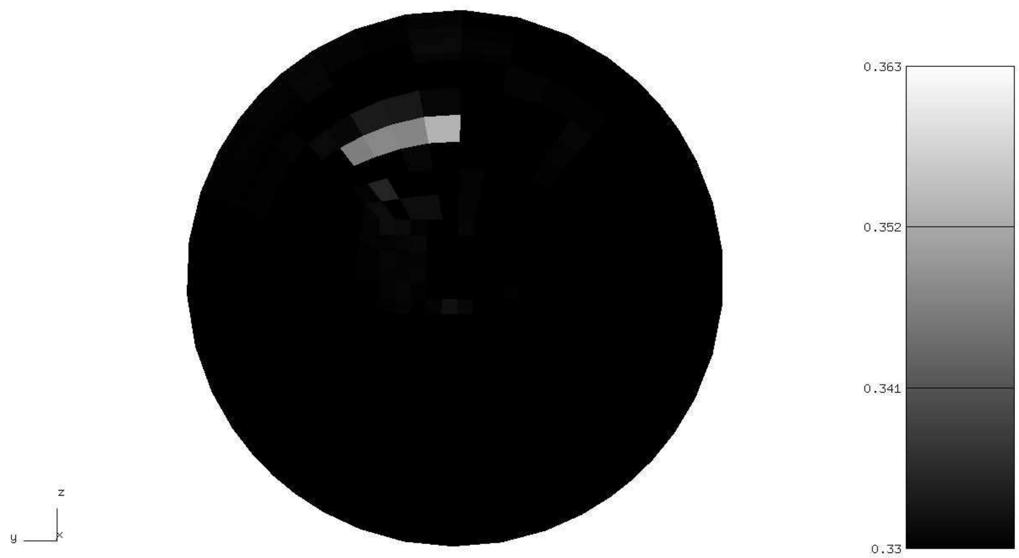

Figure 3.11: Reconstructed conductivity distribution of head when the conductivity of the inhomogeneity is 0.363 S/m.

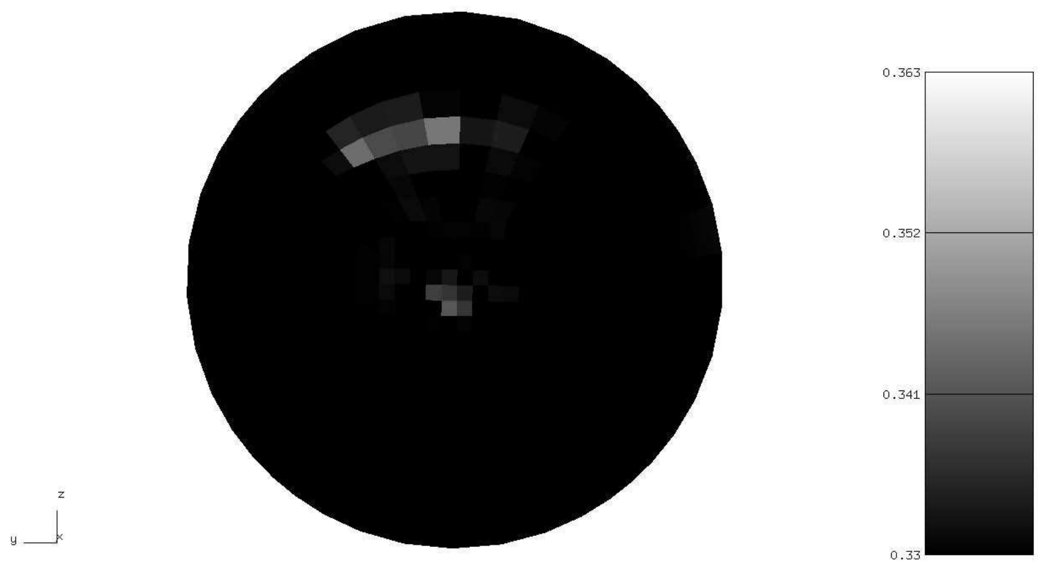

Figure 3.12: Reconstructed conductivity distribution of head when the conductivity of the inhomogeneity is 0.363 S/m. A gaussian noise with a standard deviation of 10% of maximum measurement is added to the measurements.

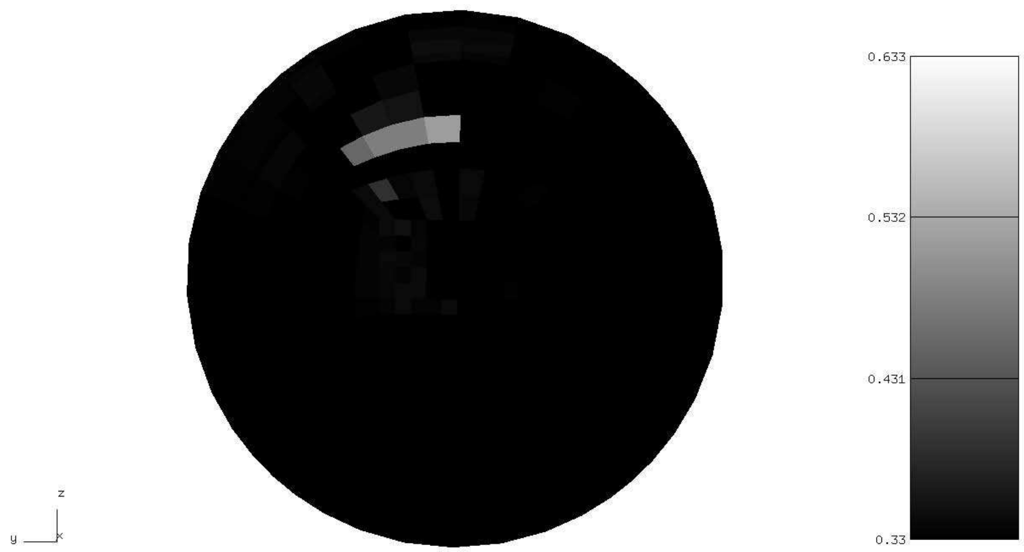

Figure 3.13: Reconstructed conductivity distribution of head when the conductivity of the inhomogeneity is 0.633 S/m.

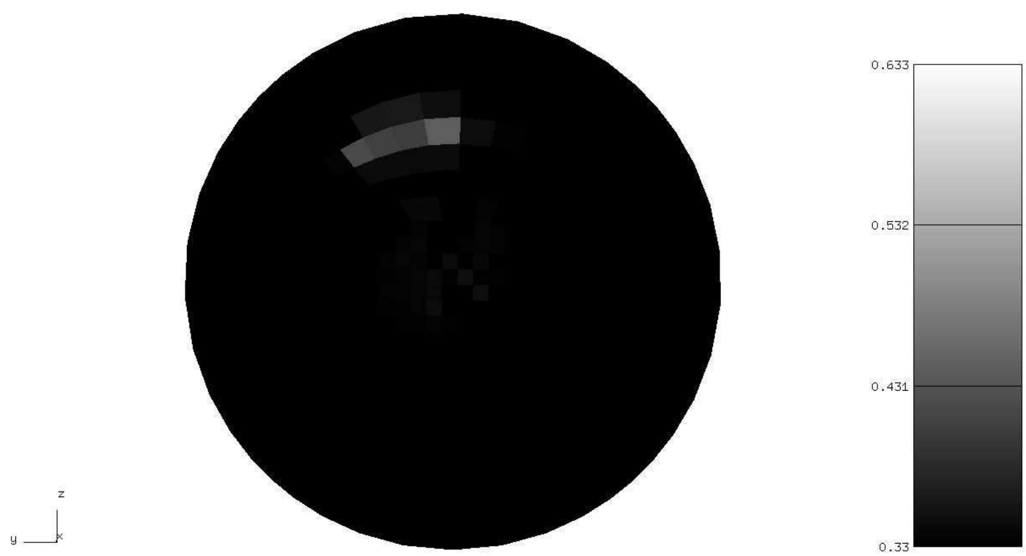

Figure 3.14: Reconstructed conductivity distribution of head when the conductivity of the inhomogeneity is 0.633 S/m. A gaussian noise with a standard deviation of 10% of maximum measurement is added to the measurements.

3.2.4 Effects of Dipole Orientation

The aim of this section is to investigate the effect of dipole orientation on the performance of inhomogeneity detection. For this purpose, 10 dipole sets, each having 3 dipoles at the same location (with x, y, z orientation) are generated (Figure 3.15). The voltages are measured using 221 electrodes attached on the head surface (Figure 3.2). The location of the inhomogeneity (shown in the top left view of Figures 3.16, 3.17, 3.18) is reconstructed by using only x, y and z oriented dipoles with no noise on the measurements. The top right views of Figures 3.16, 3.17, 3.18 show updated conductivity distribution for x oriented dipoles, the bottom left views of Figures 3.16, 3.17, 3.18 show updated conductivity distribution for y oriented dipoles. The bottom right view of Figures 3.16, 3.17, 3.18 show updated conductivity distribution for z oriented dipoles. This study shows that, identification of the inhomogeneity locations strictly depends on dipole orientation.

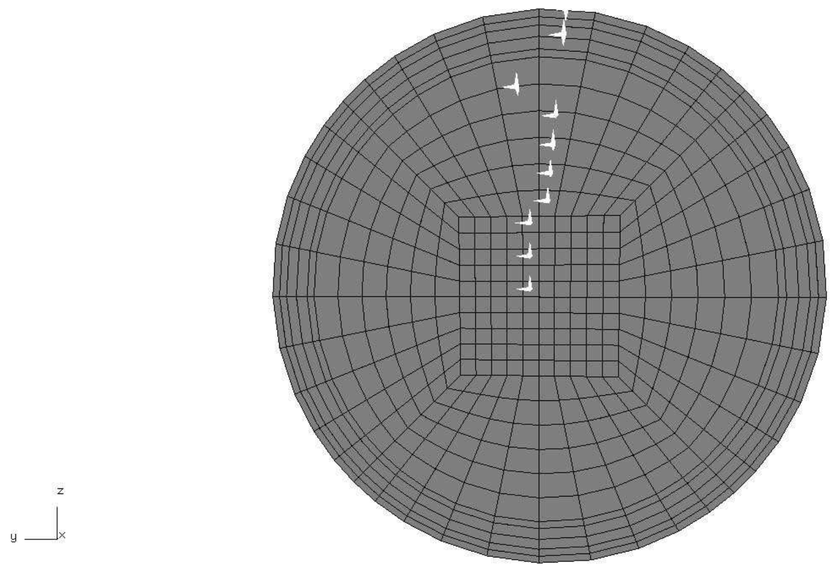

Figure 3.15: The cross section of spherical FEM mesh and positions of 10 dipole sets, each having 3 dipoles oriented in x, y, z directions.

Figure 3.16: x cross section view of the head model. The top left view is conductivity distribution of head with inhomogeneity inside, top right view is the updated conductivity distribution of head with inhomogeneity inside for x oriented dipole, bottom left view is the updated conductivity distribution of head with inhomogeneity inside for y oriented dipole, bottom right view is the updated conductivity distribution of head with inhomogeneity inside for z oriented dipole.

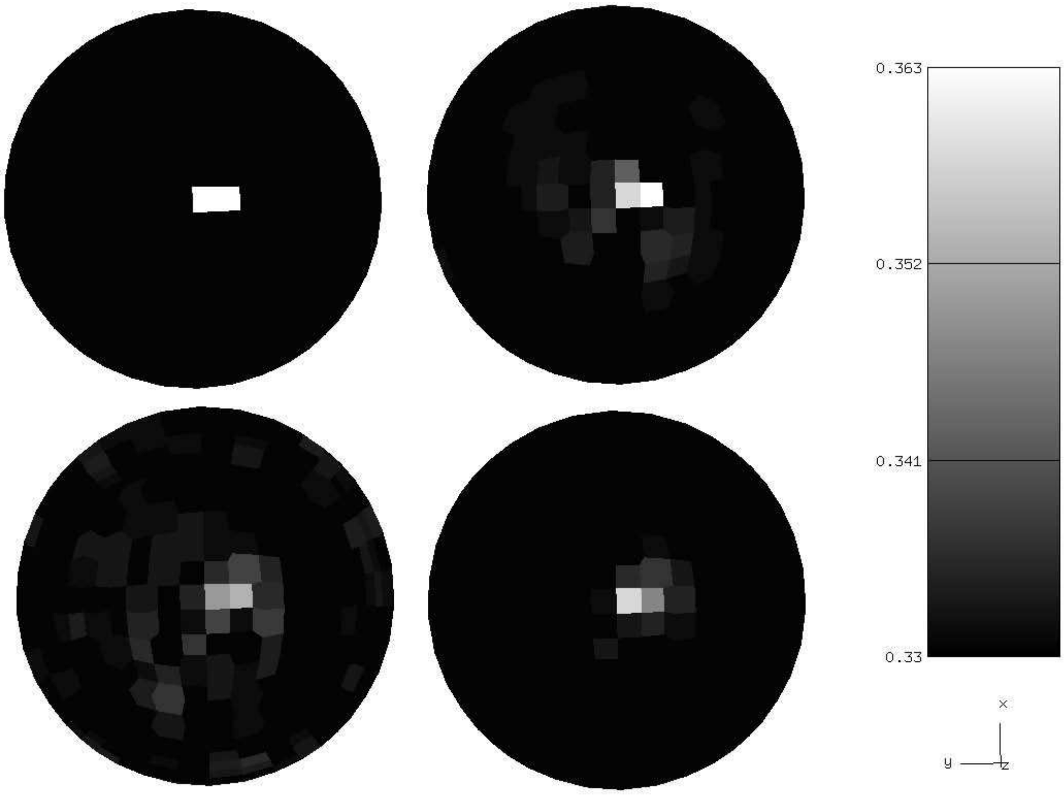

Figure 3.17: z cross section view of the head model. The top left view is conductivity distribution of head with inhomogeneity inside, top right view is the updated conductivity distribution of head with inhomogeneity inside for x oriented dipole, bottom left view is the updated conductivity distribution of head with inhomogeneity inside for y oriented dipole, bottom right view is the updated conductivity distribution of head with inhomogeneity inside for z oriented dipole.

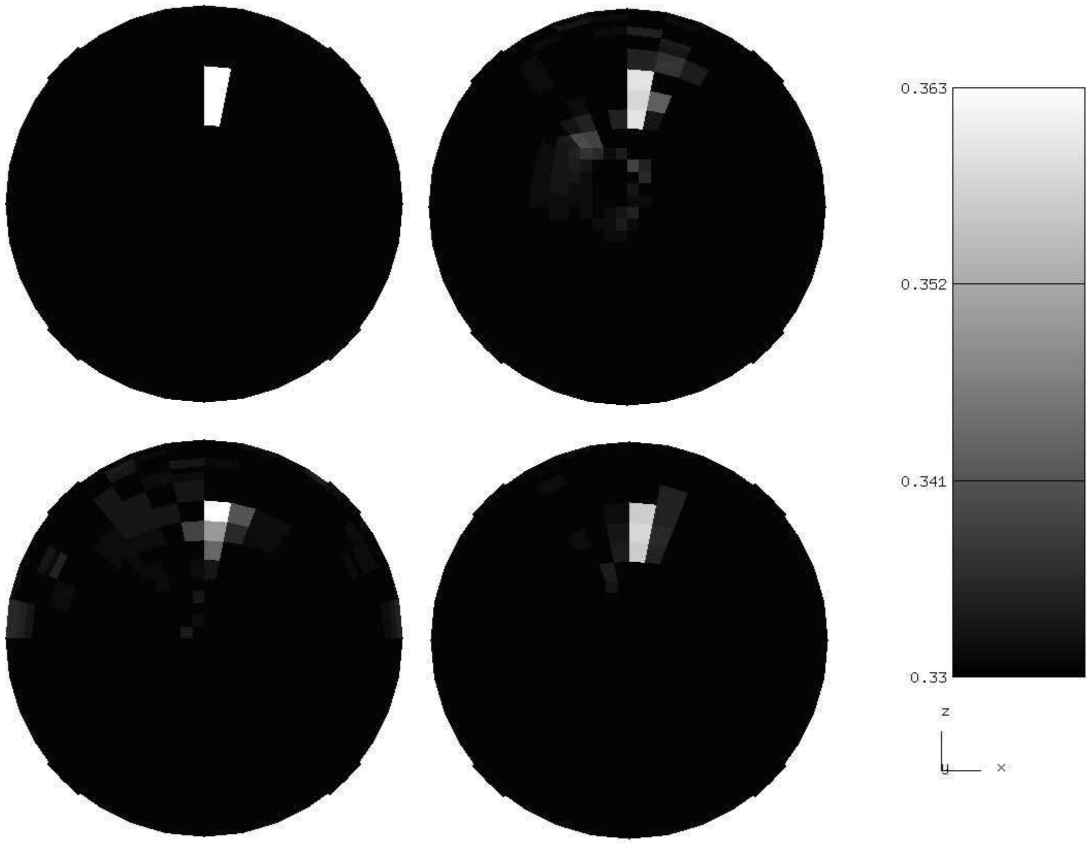

Figure 3.18: y cross section view of the head model. The top left view is conductivity distribution of head with inhomogeneity inside, top right view is the updated conductivity distribution of head with inhomogeneity inside for x oriented dipole, bottom left view is the updated conductivity distribution of head with inhomogeneity inside for y oriented dipole, bottom right view is the updated conductivity distribution of head with inhomogeneity inside for z oriented dipole.

3.2.5 Dipole with varying orientations

In this section, the location of the inhomogeneity (Figure 3.5) is reconstructed using a single dipole (Figure 3.19) located at the center of the head. The location of the dipole is fixed, however, 8 different directions are assumed in the sensitivity matrix calculations. The sensitivity matrices are appended one after another, and a larger 1768×7600 ($(221 * 8) \times 7600$) sensitivity matrix is obtained. Equation (2.1) is solved, and the location of the inhomogeneity is reconstructed (Figure 3.20) without adding any noise to the measurements. The result show that, although the location of the inhomogeneity is found, the size is not reconstructed. Better images can be reconstructed for different dipole locations, especially for dipoles closer to the inhomogeneity.

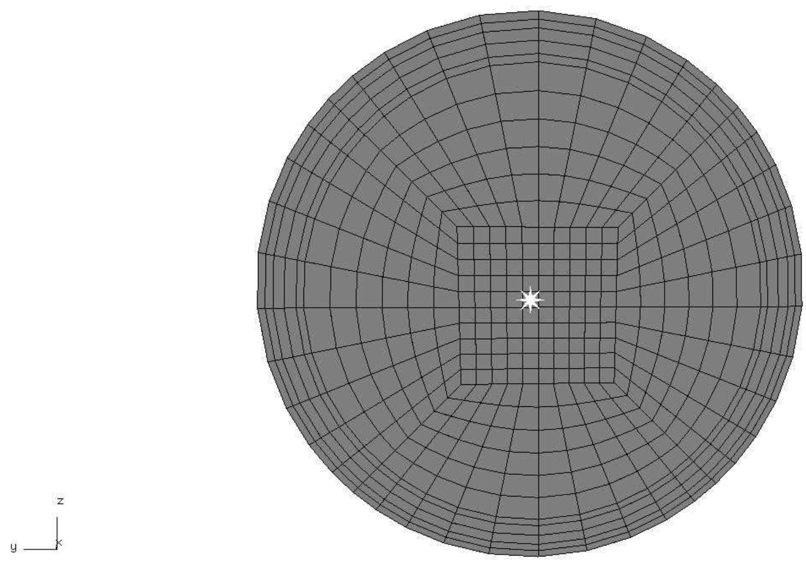

Figure 3.19: The cross section of spherical FEM mesh structure and position of one dipole with 8 different orientation.

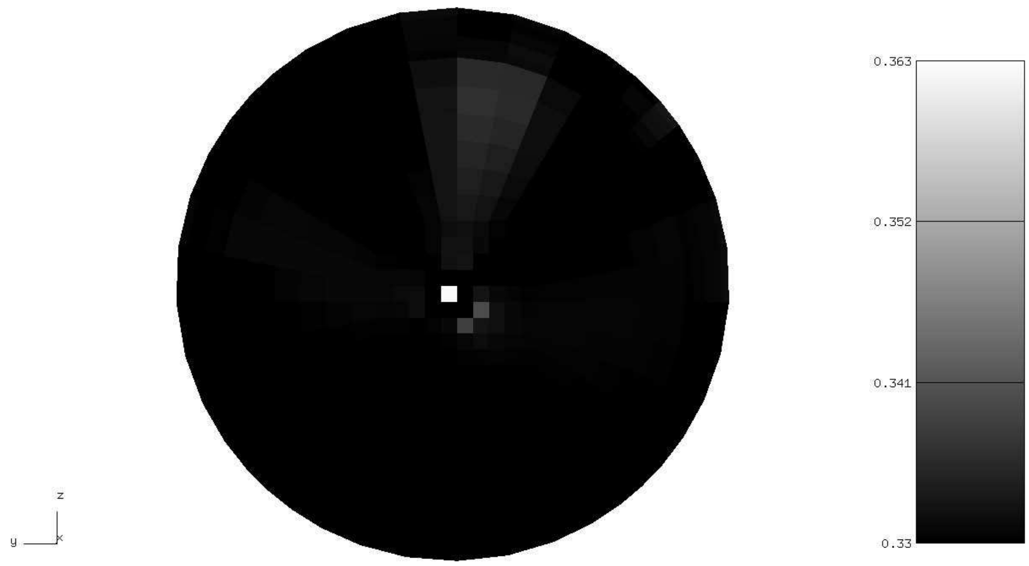

Figure 3.20: Reconstructed conductivity distribution of head with inhomogeneity inside with a conductivity of 0.363 S/m.

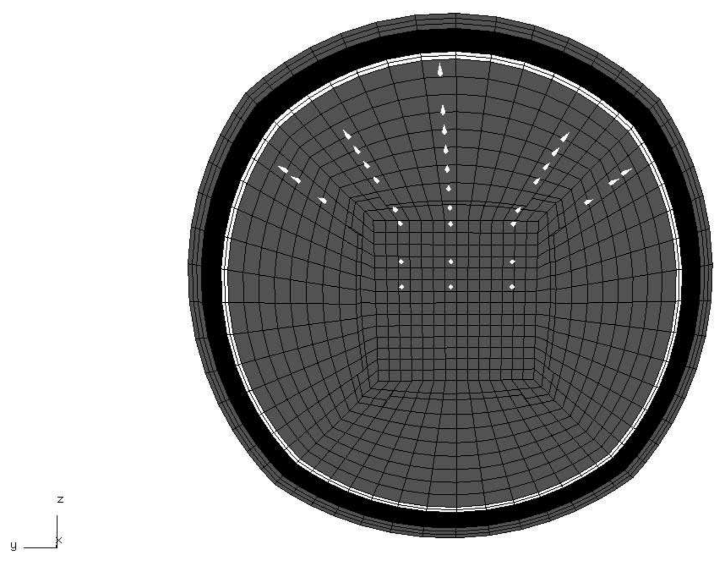

Figure 3.21: The cross section of spherical FEM mesh cross section and positions of 32 -x-oriented dipoles.

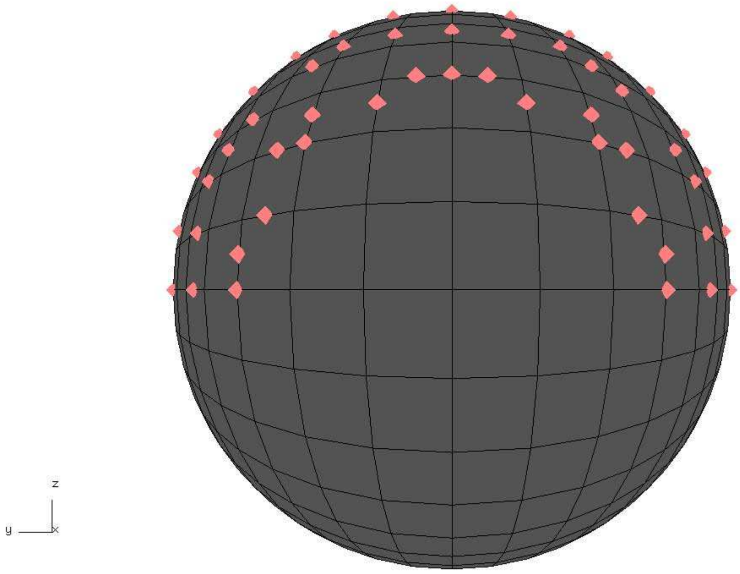

Figure 3.22: Distribution of 221 sensor positions for EEG measurements on Concentric Sphere.

3.3 Concentric Sphere

In this section, a FEM mesh consisting of 92861 nodes and 22736 elements is used to represent a 4 layer concentric sphere (Figure 3.21). Each layer in the model represents a different tissue (scalp, skull, CSF and brain) in human head, and Table 3.2 shows the initially assigned conductivity values for each tissue. 32 source configurations (sources are dipoles in x-direction, shown in Figure 3.21) in the brain are used for EEG and MEG measurements. The voltages are measured using 221 electrodes attached on the head surface (Figure 3.22) and magnetic fields are measured using 221 sensors placed nearby the head (Figure 3.22). An electrode at the occipital area is chosen as the reference electrode.

Table 3.2: The initially assigned conductivity values for brain, CSF, skull, scalp.

Layer	Conductivity Values
Brain	0.33 S/m
CSF	1.0 S/m
Skull	0.0042 S/m
Scalp	0.33 S/m

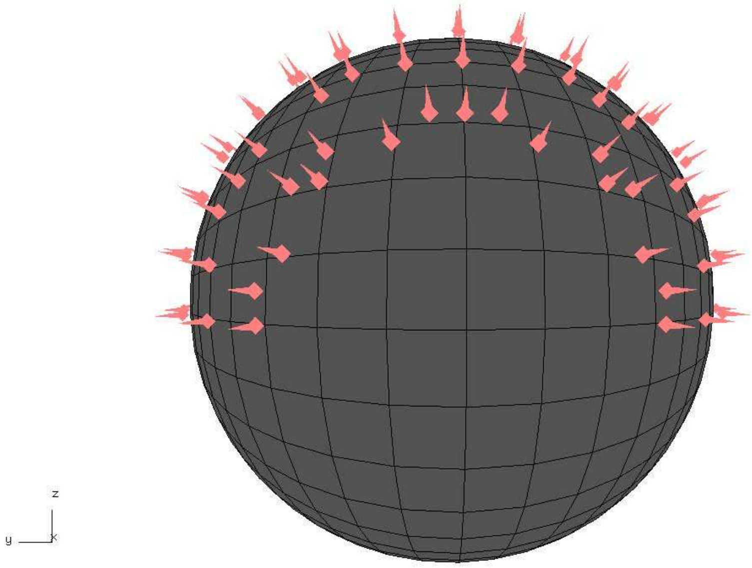

Figure 3.23: Distribution of 221 sensor positions for MEG measurements on Concentric Sphere.

3.3.1 Computing Tissue Conductivities of the four-layer head model (4 unknowns)

In this section, all elements in the same tissue are assumed to have the same conductivity value. Table 3.2 presents the initially assigned conductivity values, and Table 3.3 presents the realistic values for tissue conductivities. The conductivity of four tissues are the unknowns (i.e., the elements corresponding to the same tissue are grouped), and aim is to compute the conductivity of these tissues. For this purpose, 32 dipoles (Figure 3.21) in the brain are used for EEG and MEG measurements. The voltages are measured using 221 electrodes attached on the head surface (Figure 3.22) and magnetic fields are measured using 221 sensors placed nearby the head (Figure 3.22). Simulations are performed using noisy (A gaussian noise with a standard deviation of 10% of maximum measurement) and noise-free evoked potentials and evoked magnetic fields.

Note that, the dimension of sensitivity matrix is $m \times n$ for potential measurements and $(3{*}m) \times n$ for magnetic fields measurements, where m is the number of sensors-n is the total number of elements. Since the conductivity value is assumed to be constant in the same tissue, the columns in the sensitivity matrix corresponding to the elements of the same tissue can be added. Thus, the dimension of sensitivity matrix can be reduced to $m \times l$ for potential measurements and $(3 * m) \times l$ for magnetic fields measurements, where l is the number of layers (or unknowns).

In Tables 3.4, 3.5, 3.6, 3.7, the calculated new conductivity values of the four tissues are presented. Results show that, using noise free potential measurements, the conductivity of tissues are calculated accurately when the change in the conductivity is 0.1% and 1%; and with an error of 1% when the change in the conductivity is 10%. When noise is added to potential mesurements, conductivity change of 1% gives the most accurate result. Tissue conductivities for skull and brain can be calculated using the magnetic field noise-free measurements. If noise is added to magnetic field measurements, conductivity of the tissues can not be calculated.

Table 3.3: The initially assigned conductivity values increased by 0.1%, 1% and 10%.

	0.1%	1%	10%
Brain	0.33033	0.3333	0.363
CSF	1.001	1.01	1.1
Skull	0.0042042	0.004242	0.00462
Scalp	0.33033	0.3333	0.363

Table 3.4: The calculated conductivity values. Potential difference obtained from 221 electrodes are used.

	0.1%	1%	10%
Brain	0.33033	0.3333	0.3600
CSF	1.0011	1.0099	1.0981
Skull	0.0042042	0.0042418	0.0046005
Scalp	0.33033	0.3333	0.3613

Table 3.5: The calculated conductivity values. Potential difference obtained from 221 electrodes are used. A gaussian noise with a standard deviation of 10% of maximum measurement is added to the measurements.

	0.1%	1%	10%
Brain	0.33011	0.3333	0.3600
CSF	1.00081	1.013	1.0947
Skull	0.0042048	0.0042481	0.0046098
Scalp	0.3297	0.33377	0.3611

Table 3.6: The calculated conductivity values. Magnetic fields difference obtained from 221 sensors are used.

	0.1%	1%	10%
Brain	0.33031	0.33303	0.358
CSF	1.000	0.99992	0.9992
Skull	0.0042042	0.004241	0.0046
Scalp	0.3333	0.3633	0.6631

Table 3.7: The calculated conductivity values. Magnetic fields difference obtained from 221 number of sensors are used. A gaussian noise with a standard deviation of 10% of maximum measurement is added to the measurements.

	0.1%	1%	10%
Brain	0.3296	0.3325	0.3572
CSF	0.9938	1.0024	0.9982
Skull	0.00424	0.004348	0.004338
Scalp	0.341	0.3667	0.6715

3.3.2 Reconstructing the conductivity distribution of the four-layer head model (Many unknowns)

In this section, although initial and actual conductivity distribution of elements in the same tissue is assumed to be uniform, the reconstructed conductivity distribution does not have to be uniform. Thus, the elements corresponding to the same tissues can not grouped. Since, number of unknown is number of elements of a specific tissue (i.e., 13328 for brain, 2352 for CSF, 3528 for scalp, and 3528 for skull), dimension of the sensitivity matrix is reduced to $m \times 13328$ for brain, $m \times 2352$ for CSF, $m \times 3528$ for scalp and $m \times 3528$ for skull (for magnetic fields measurements m must be replaced by $3 * m$). Simulations are performed using the dipole, sensor and noise information specified in the previous section, and the percentage RDM values (in Tables 3.8, 3.9, 3.10, 3.11) are presented to investigate the performance of the approach.

Results show that, RDM values increase with the increase in the conductivity when noise-free potentials and magnetic filds measurements are used. When noise is added to potential measurements, scalp is the only tissue that does not obey this monotonic increase. For MEG noisy measurements, brain and CSF are the only tissues that RDM values increase as conductivity increases.

Table 3.8: The computed RDM values. Potential difference obtained from 221 electrodes are used.

	0.1%	1%	10%
Brain	0.0995	0.9812	9.0093
CSF	0.0943	1.0680	10.3302
Skull	0.1237	1.1059	10.0629
Scalp	0.0445	0.3601	3.2663

Table 3.9: The computed RDM values. Potential difference obtained from 221 electrodes are used. A gaussian noise with a standard deviation of 10% of maximum measurement is added to the measurements.

	0.1%	1%	10%
Brain	0.1072	0.9943	9.6621
CSF	0.0999	0.9901	10.7137
Skull	0.5274	1.1130	11.6413
Scalp	3.2983	1.5687	13.5717

Table 3.10: The computed RDM values. Magnetic fields difference obtained from 221 sensors are used.

	0.1%	1%	10%
Brain	0.1107	1.3316	11.7688
CSF	0.0963	0.9861	9.0812
Skull	0.1205	0.9574	8.2335
Scalp	0.1363	1.3726	12.5460

Table 3.11: The computed RDM values. Magnetic fields difference obtained from 221 number of sensors are used. A gaussian noise with a standard deviation of 10% of maximum measurement is added to the measurements.

	0.1%	1%	10%
Brain	0.1002	0.9901	9.0909
CSF	0.3471	1.1800	9.1346
Skull	37.2783	44.3530	31.2816
Scalp	12.1364	10.8696	14.2191

3.3.3 Inhomogeneity Imaging

The proposed approach can also be used as a new imaging modality. The aim of this section is to investigate the performance of this technique using simulations. The goal of this simulation is to distinguish a inhomogeneity in the brain of a four-layer spherical head.

The initial head model is a four-layer spherical head with a homogeneous brain. For a given set of source configuration, the forward problem is solved twice: 1) using the model with a inhomogeneity in the brain, and 2) using the model with homogeneous brain. The potential differences obtained from the potentials of the two head model are used in Equation (2.1). A least squares QR (lsqr)-solution is obtained to identify the change in conductivity in the inhomogeneity region of the brain. Similarly, magnetic fields calculated for the two head models are used in Equation (2.2) and changes in the conductivity are reconstructed. The effect of inhomogeneity location on the imaging performance is investigated for 5 different inhomogeneity positions (Figures 3.24, 3.29, 3.34, 3.39, 3.44) using noisy (A gaussian noise with a standard deviation of 1% of maximum measurement is added to the measurements.) and noise-free measurements. First, the conductivity distribution of brain is reconstructed using the potential measurements without adding any noise. Figures 3.25, 3.30, 3.35, 3.40, 3.45) show that, the location of inhomogeneity is distinguished. Next, the conductivity distribution of brain is reconstructed using the potential measurements by adding noise (Figures 3.26, 3.31, 3.36, 3.41, 3.46)). However, the location of the inhomogeneity are identified, there are small perturbed regions in the center of the head. After, the conductivity distribution of brain is reconstructed using the magnetic fields without adding any noise. Figures 3.27, 3.32, 3.37, 3.42, 3.47 show that the location of the inhomogeneity is not distinguished accurately, since there are perturbed regions in the vicinity of the inhomogeneities. Finally, the conductivity distribution of brain is reconstructed using the magnetic fields with adding any noise. As the Figures 3.28, 3.33, 3.38, 3.43, 3.48 show that the location of inhomogeneities can not be identified. There are perturbations in the dipole locations.

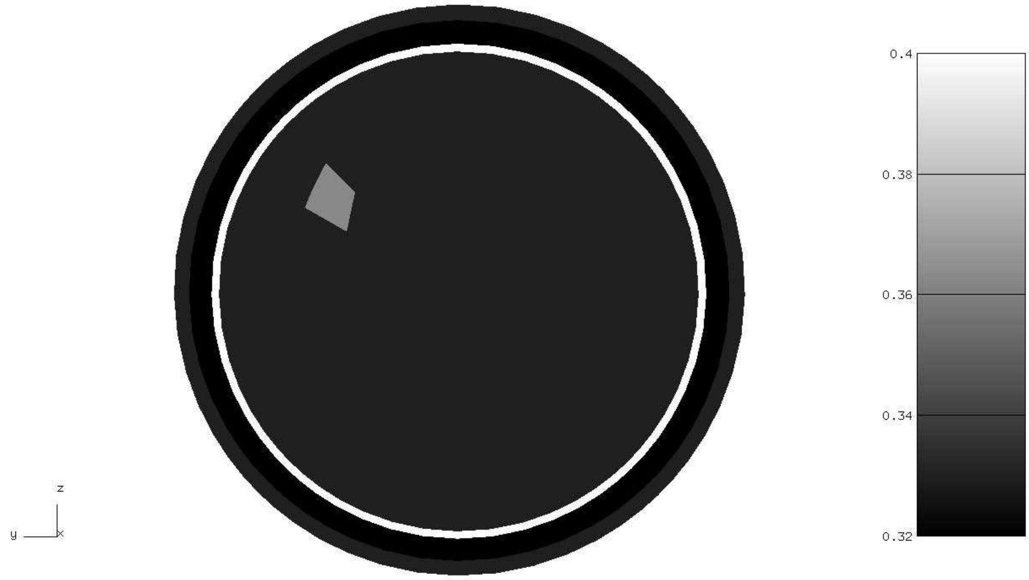

Figure 3.24: Realistic conductivity distribution of head with inhomogeneity inside (white region).

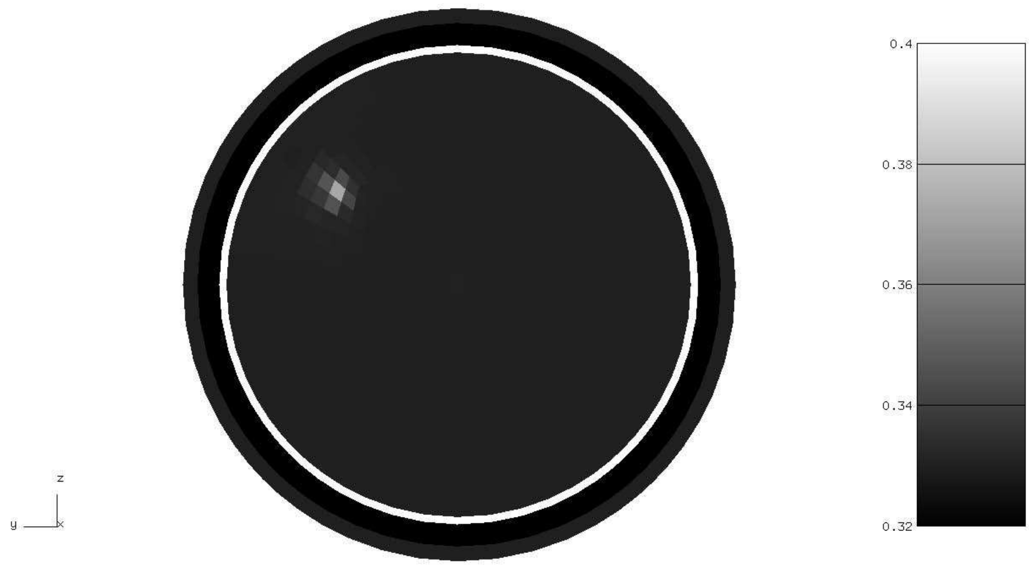

Figure 3.25: Reconstructed conductivity distribution of head with a inhomogeneity inside. Potential difference obtained from 221 electrodes are used.

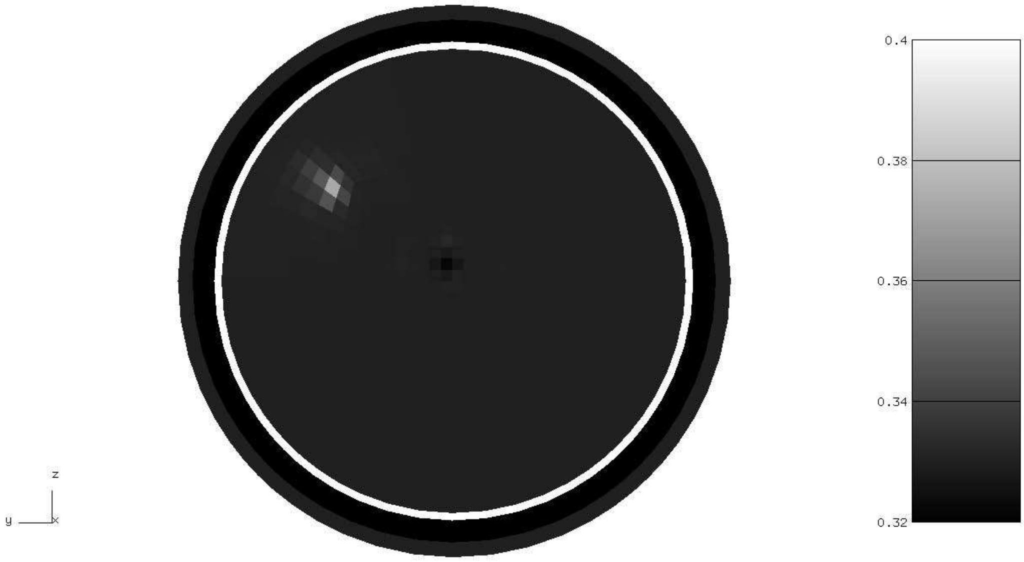

Figure 3.26: Reconstructed conductivity distribution of head with a inhomogeneity inside. Potential difference obtained from 221 are used. A gaussian noise with a standard deviation of 1% of maximum measurement is added to the measurements.

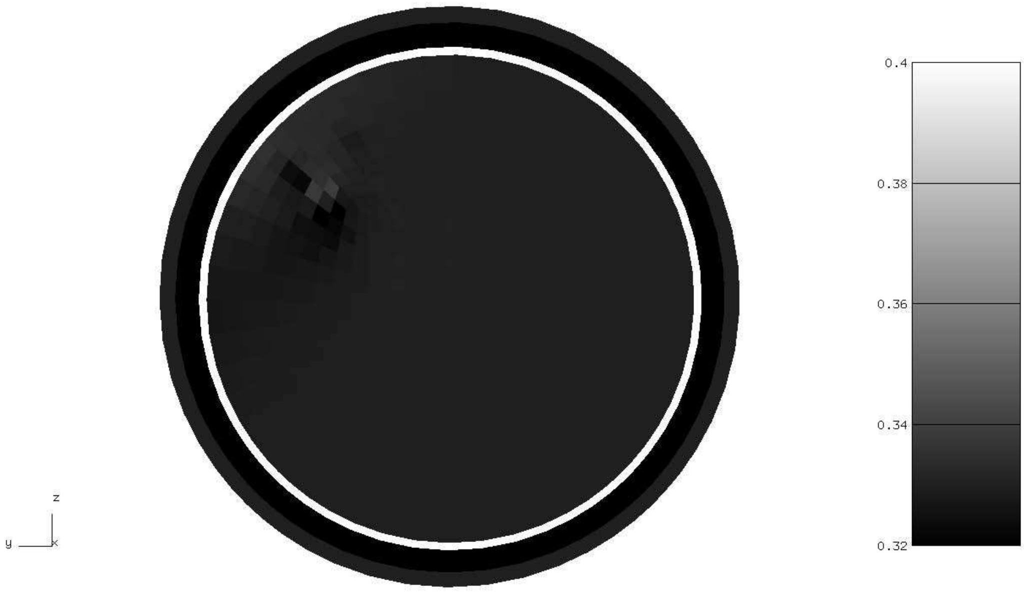

Figure 3.27: Reconstructed conductivity distribution of head with a inhomogeneity inside. Magnetic fields difference obtained from 221 sensors are used.

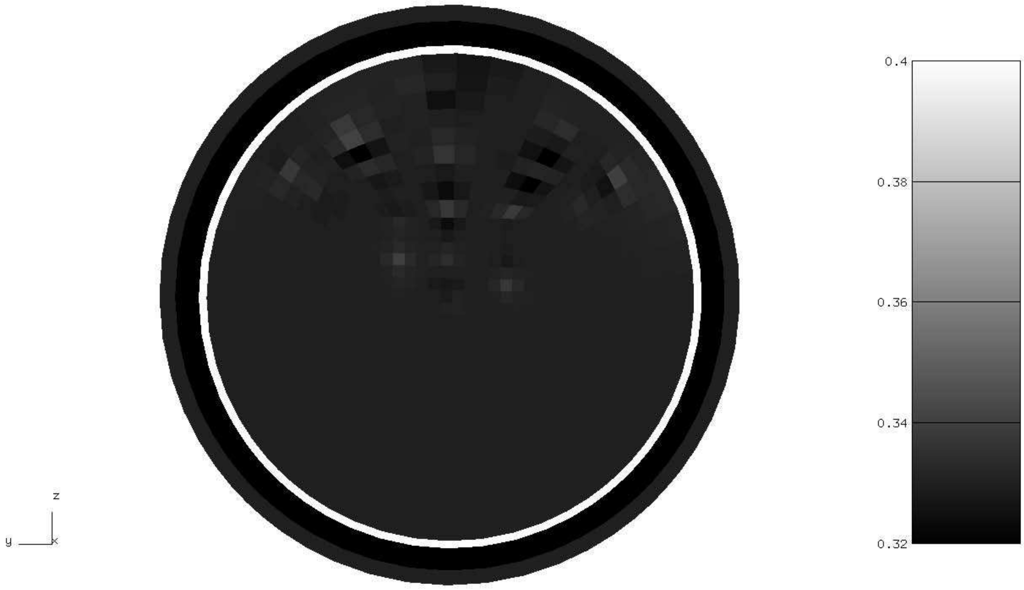

Figure 3.28: Reconstructed conductivity distribution of head with a inhomogeneity inside. Magnetic fields difference obtained from 221 sensors are used. A gaussian noise with a standard deviation of 1% of maximum measurement is added to the measurements.

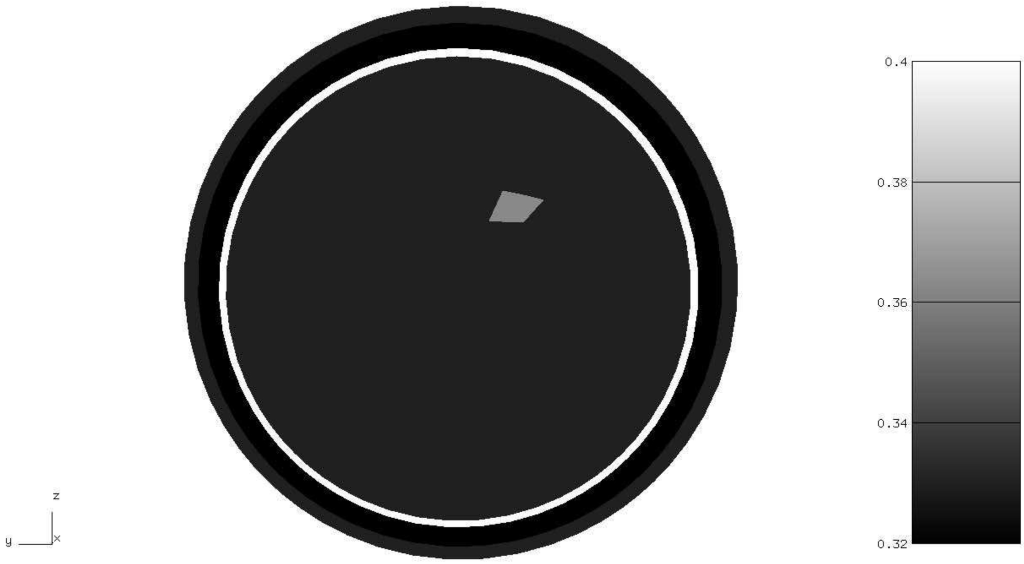

Figure 3.29: Realistic conductivity distribution of head with inhomogeneity inside (white region).

Figure 3.30: Reconstructed conductivity distribution of head with a inhomogeneity inside. Potential difference obtained from 221 electrodes are used.

Figure 3.31: Reconstructed conductivity distribution of head with a inhomogeneity inside. Potential difference obtained from 221 electrodes are used. A gaussian noise with a standard deviation of 1% of maximum measurement is added to the measurements.

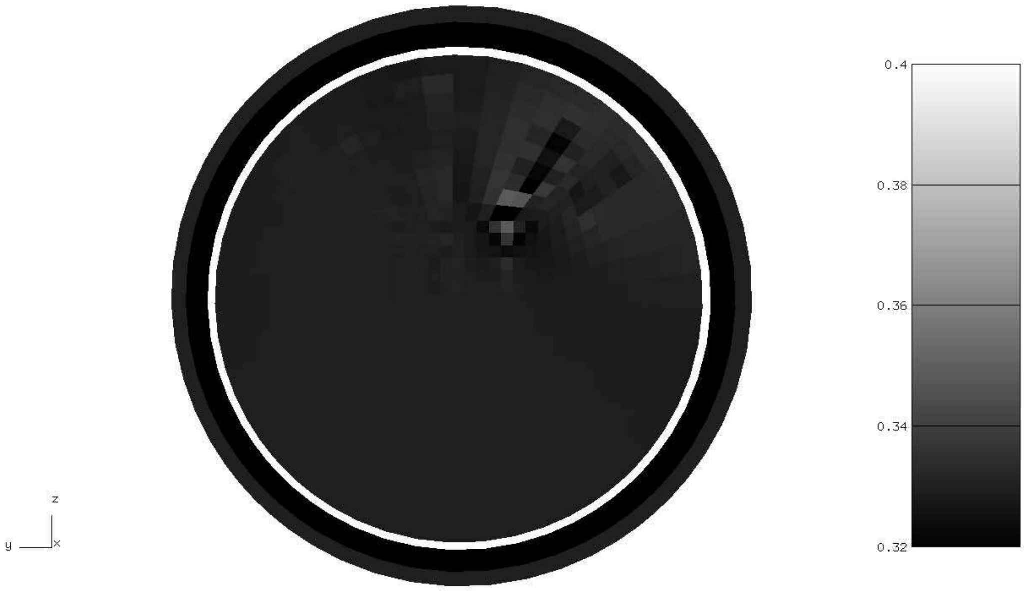

Figure 3.32: Reconstructed conductivity distribution of head with a inhomogeneity inside. Magnetic fields difference obtained from 221 sensors are used.

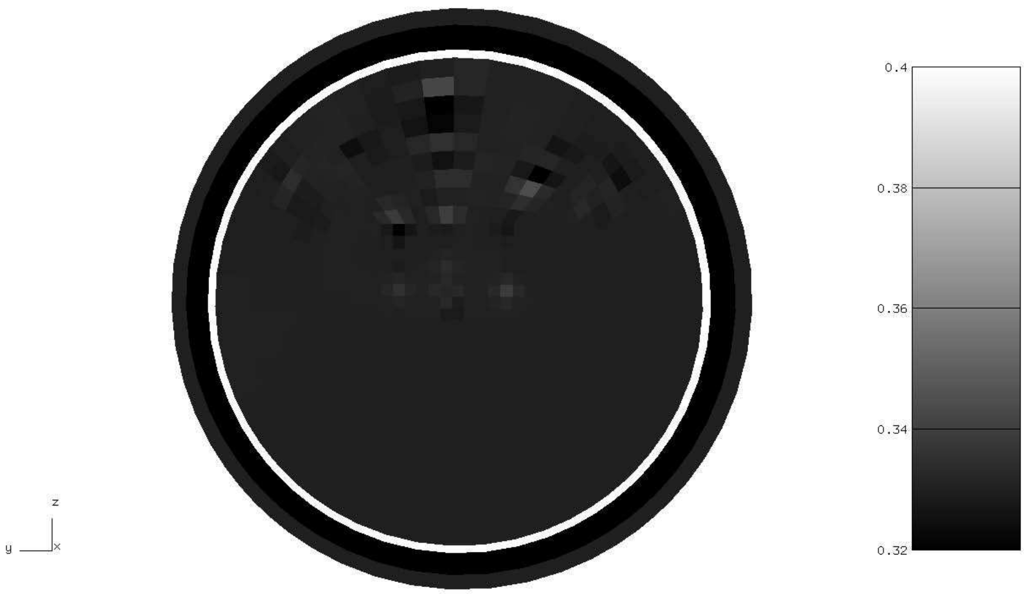

Figure 3.33: Reconstructed conductivity distribution of head with a inhomogeneity inside. Magnetic fields difference obtained from 221 sensors are used. A gaussian noise with a standard deviation of 1% of maximum measurement is added to the measurements.

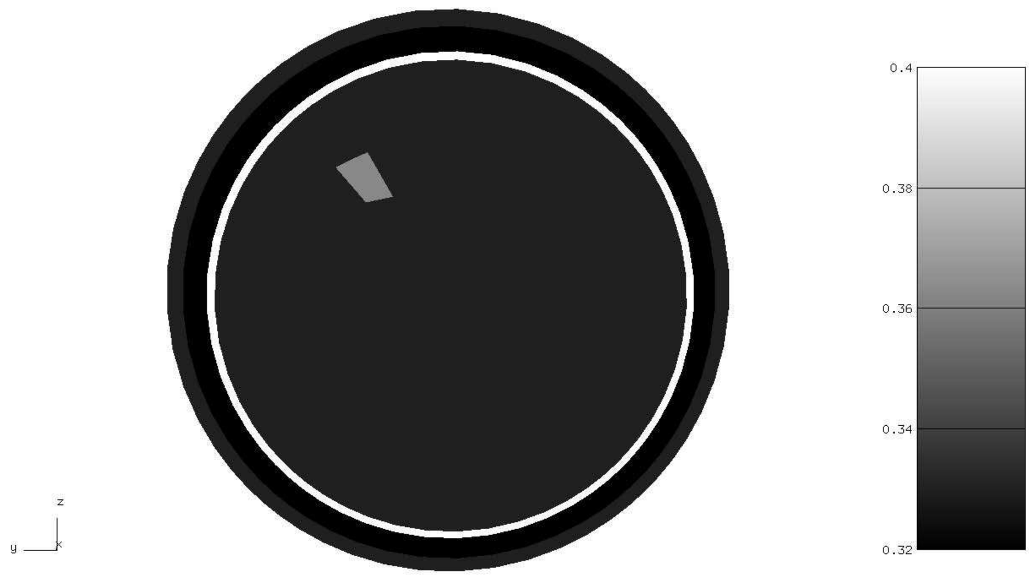

Figure 3.34: Realistic conductivity distribution of head with inhomogeneity inside (white region).

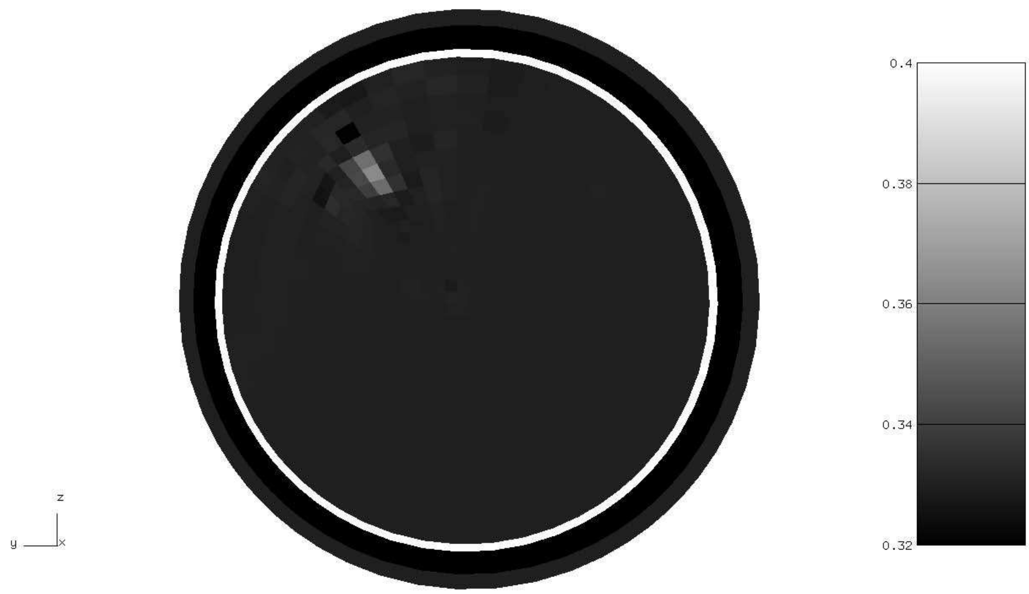

Figure 3.35: Reconstructed conductivity distribution of head with a inhomogeneity inside. Potential difference obtained from 221 electrodes are used.

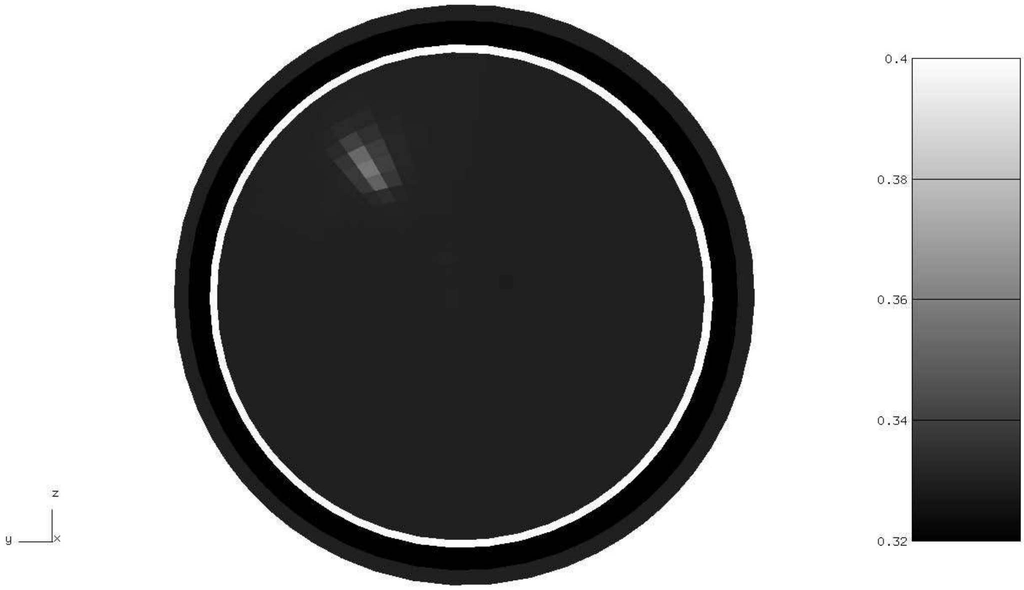

Figure 3.36: Reconstructed conductivity distribution of head with a inhomogeneity inside. Potential difference obtained from 221 electrodes are used. A gaussian noise with a standard deviation of 1% of maximum measurement is added to the measurements.

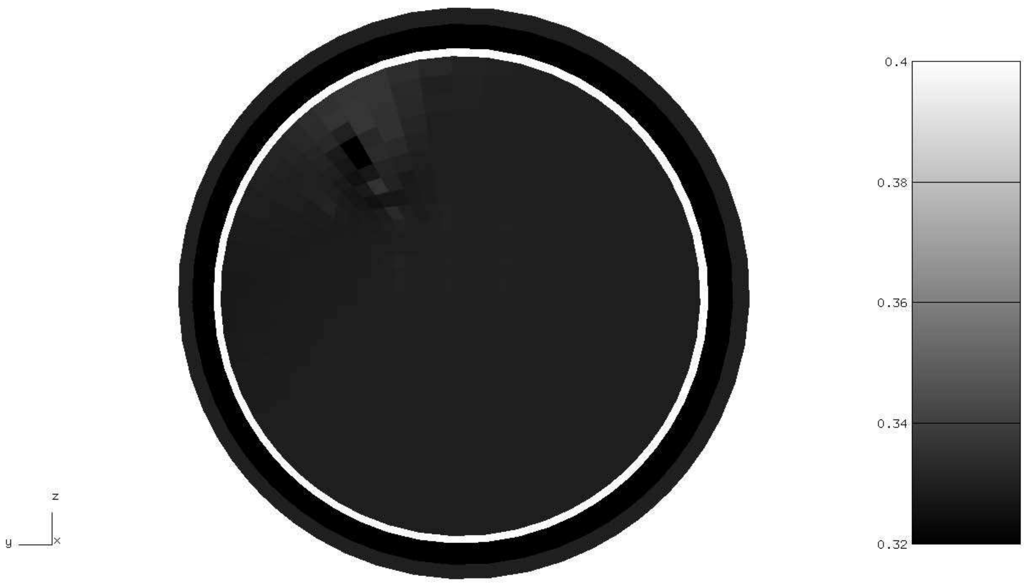

Figure 3.37: Reconstructed conductivity distribution of head with a inhomogeneity inside. Magnetic fields difference obtained from 221 sensors are used.

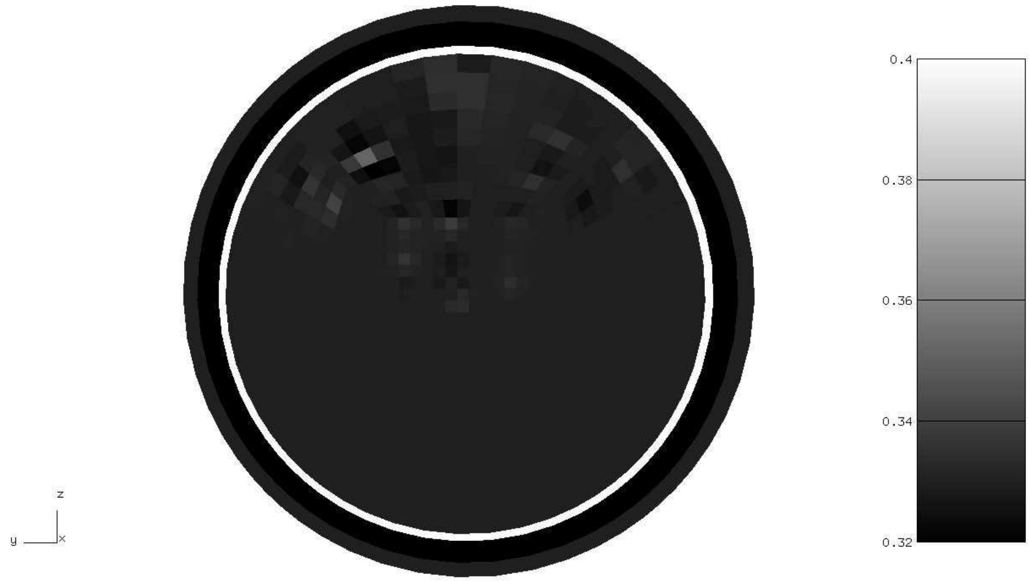

Figure 3.38: Reconstructed conductivity distribution of head with a inhomogeneity inside. Magnetic fields difference obtained from 221 sensors are used. A gaussian noise with a standard deviation of 1% of maximum measurement is added to the measurements.

Figure 3.39: Realistic conductivity distribution of head with inhomogeneity inside (white region).

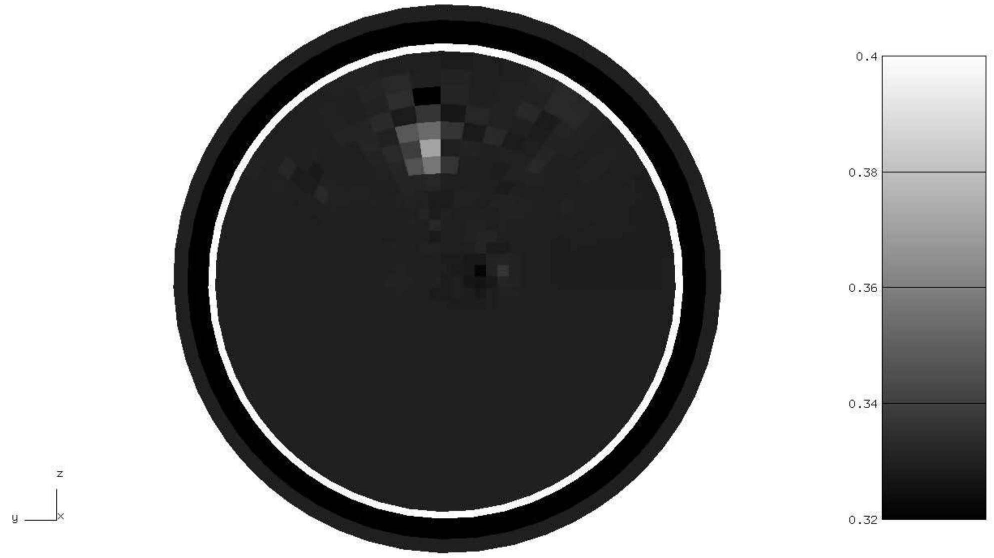

Figure 3.40: Reconstructed conductivity distribution of head with a inhomogeneity inside. Potential difference obtained from 221 electrodes are used.

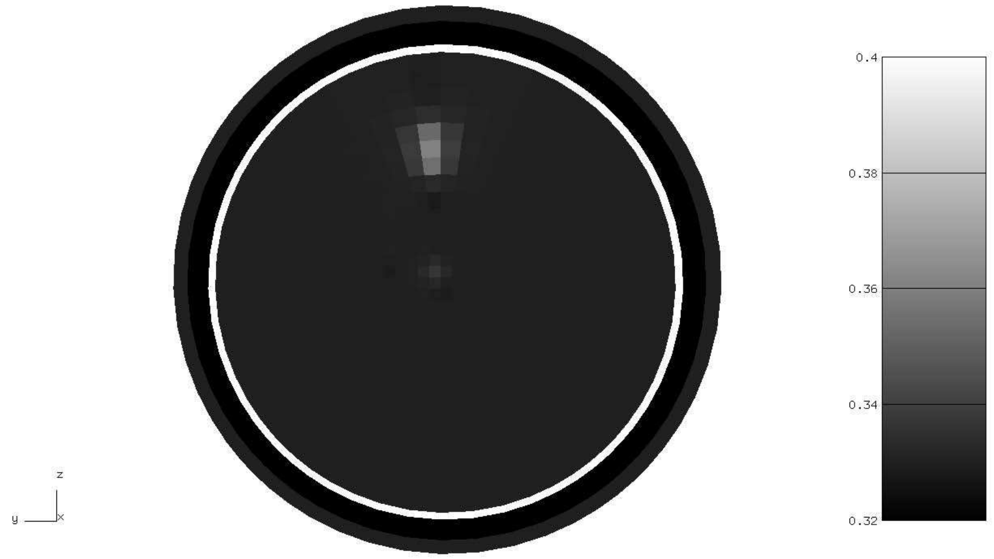

Figure 3.41: Reconstructed conductivity distribution of head with a inhomogeneity inside. Potential difference obtained from 221 electrodes are used. A gaussian noise with a standard deviation of 1% of maximum measurement is added to the measurements.

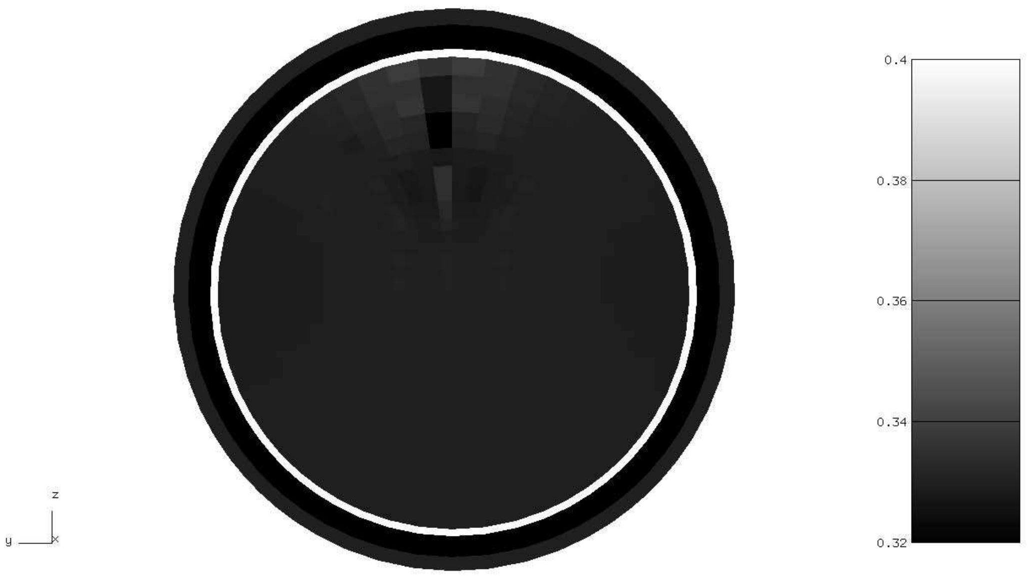

Figure 3.42: Reconstructed conductivity distribution of head with a inhomogeneity inside. Magnetic fields difference obtained from 221 sensors are used.

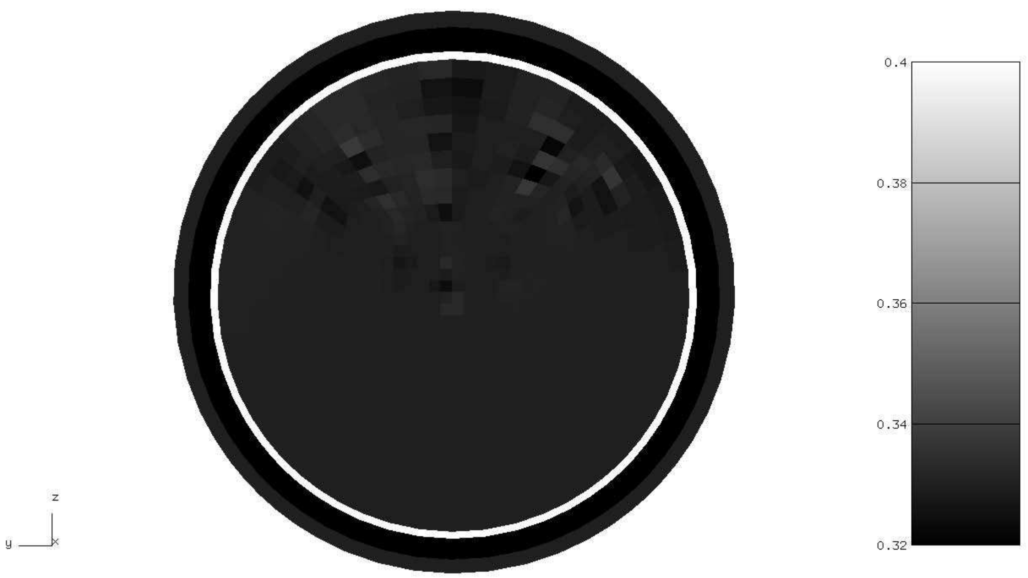

Figure 3.43: Reconstructed conductivity distribution of head with a inhomogeneity inside. Magnetic fields difference obtained from 221 number of sensors are used. A gaussian noise with a standard deviation of 1% of maximum measurement is added to the measurements.

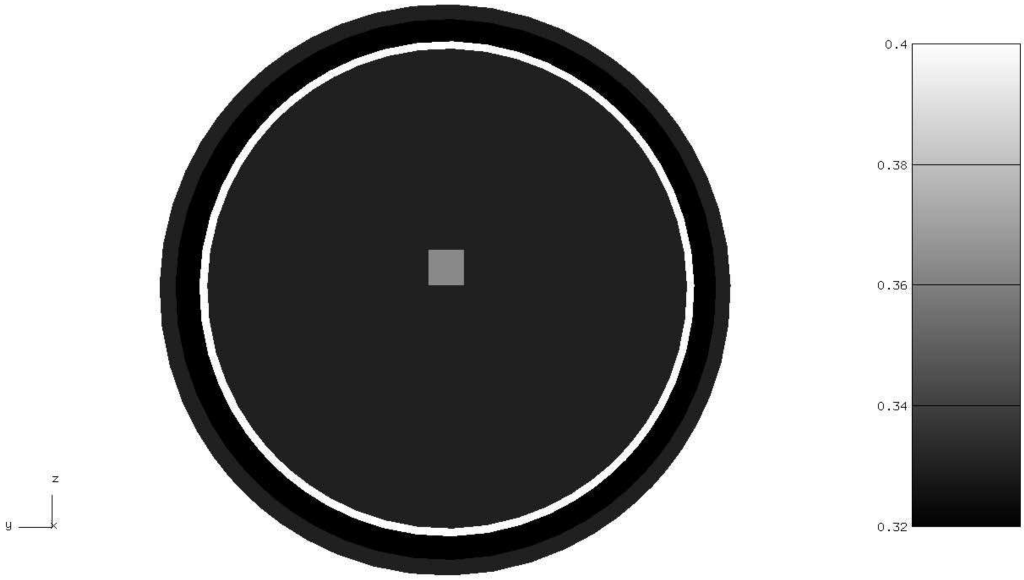

Figure 3.44: Realistic conductivity distribution of head with inhomogeneity inside (white region).

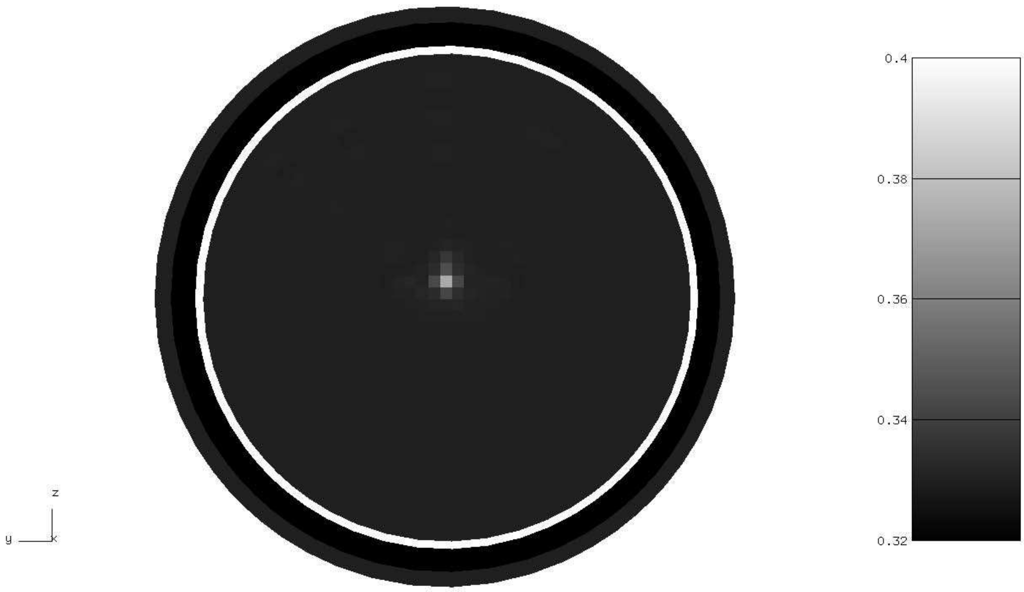

Figure 3.45: Reconstructed conductivity distribution of head with a inhomogeneity inside. Potential difference obtained from 221 electrodes are used.

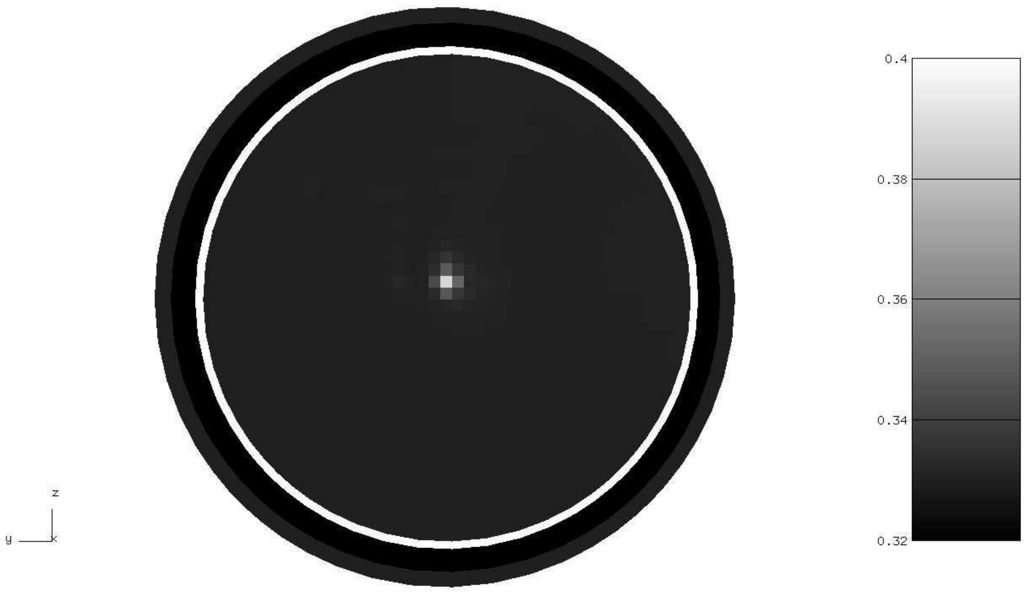

Figure 3.46: Reconstructed conductivity distribution of head with a inhomogeneity inside. Potential difference obtained from 221 electrodes are used. A gaussian noise with a standard deviation of 1% of maximum measurement is added to the measurements.

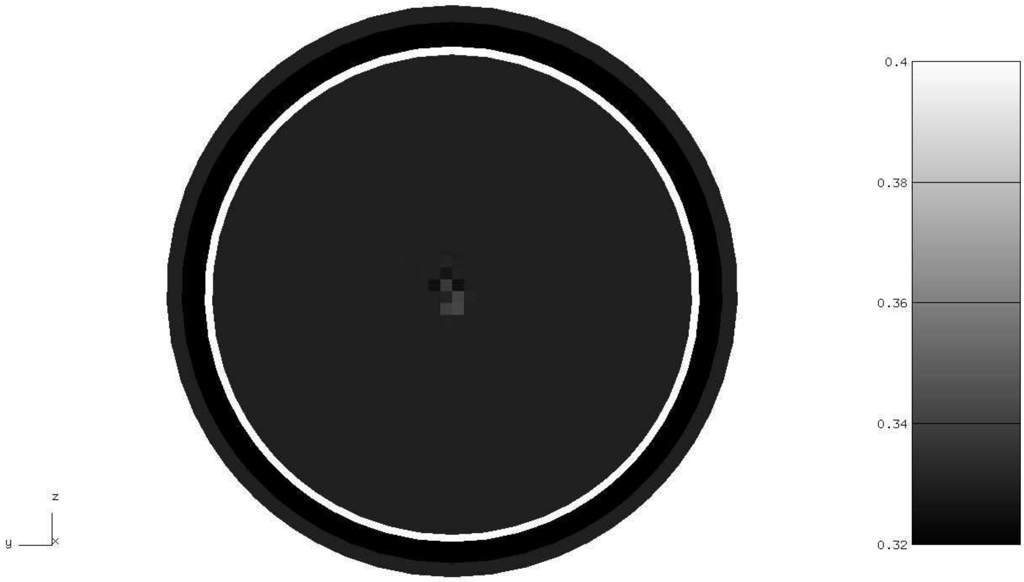

Figure 3.47: Reconstructed conductivity distribution of head with a inhomogeneity inside. Magnetic fields difference obtained from 221 sensors are used.

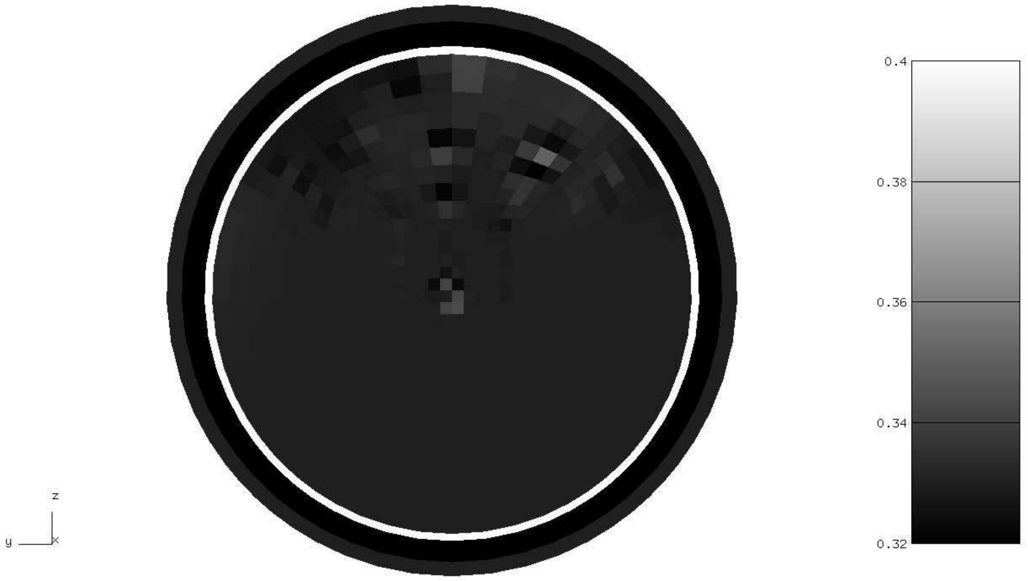

Figure 3.48: Reconstructed conductivity distribution of head with a inhomogeneity inside. Magnetic fields difference obtained from 221 sensors are used. A gaussian noise with a standard deviation of 1% of maximum measurement is added to the measurements.

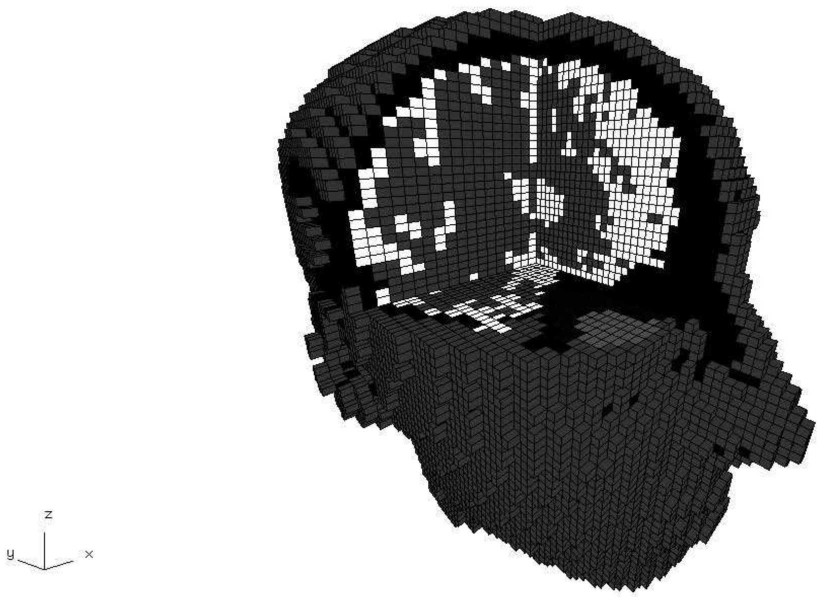

Figure 3.49: Realistic FEM mesh structure are composed of rectangular grids.

3.4 Realistic Head Model

In this section, a FEM mesh consisting of 118193 nodes and 108514 elements is used to represent a 6 layer realistic head model (Figure 3.49). 6 tissues are used in the model (scalp, skull, CSF, brain, fat and eye), and Table 3.12 shows the initially assigned conductivity values for each tissue. The boundary of the tissues are obtained by using segmentation algorithms to Dr. Zeynep Akalın's MRI images [25]. 14 dipole sets, each having 3 dipoles at the same location (with x, y, z orientation) (Figure 3.50) in the brain are used for EEG and MEG measurements. The voltages are measured using 25 electrodes attached on the head surface (Figure 3.50) and magnetic fields are measured using 25 sensors placed nearby the head (Figure 3.50). An electrode at the occipital area is chosen as the reference electrode. Because of the computational limitations, 25 sensors are used instead of 221 sensors.

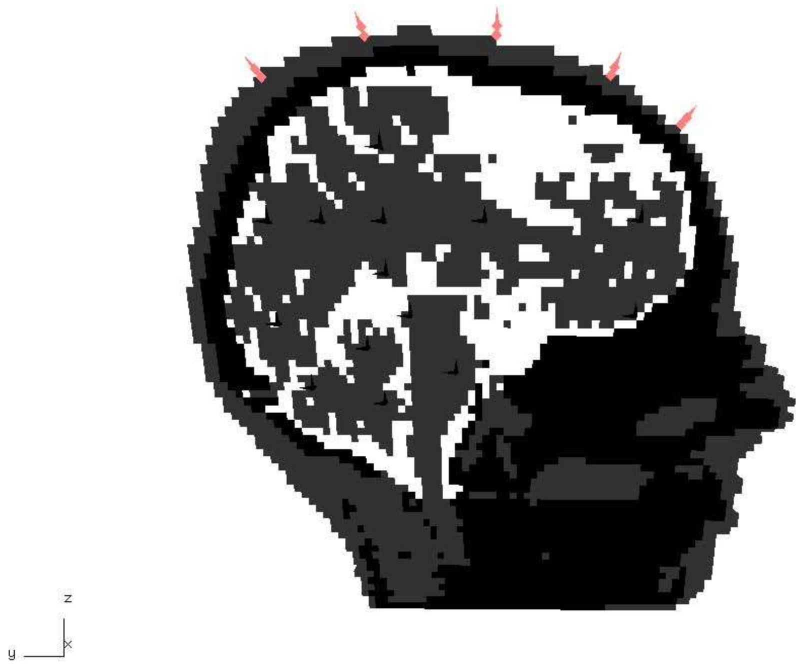

Figure 3.50: Location of 14 dipole sets, each having 3 dipoles at the same location, 25 potential and magnetic sensors on the realistic head model.

Table 3.12: The initially assigned conductivity values for brain, CSF, skull, scalp, fat, eye.

Layer	Conductivity Values
Brain	0.2 S/m
CSF	1.0 S/m
Skull	0.005 S/m
Scalp	0.2 S/m
Fat	0.02 S/m
Eye	0.3 S/m

3.4.1 Computing Tissue Conductivities of the realistic head model (4 unknowns)

In this section, all the elements in the same tissue are assumed to have the same conductivity value. Table 3.12 and Table 3.13 present the initial and actual conductivity values of the tissues. Although there are 6 tissues in the model, the fat and eye tissues are not included in the conductivity computations. Then, the conductivity of the four tissues (brain, CSF, scalp, skull) are the unknowns (i.e., the elements corresponding to the same tissue are grouped), and aim is to compute the conductivity of these tissues. For this purpose, 14 dipole sets, each having 3 dipoles at the same location (Figure 3.50) in the brain are used for EEG and MEG measurements. The voltages are measured using 25 electrodes attached on the head surface (Figure 3.50) and magnetic fields are measured using 25 sensors placed nearby the head (Figure 3.50). Simulations are performed using noisy (A gaussian noise with a standard deviation of 10% of maximum measurement is added to the measurements.) and noise-free evoked potentials and evoked magnetic fields.

In Tables 3.14, 3.15, 3.16, 3.17, the calculated conductivity values of the four tissues are presented. Results show that, conductivity of tissues (except for scalp) can be calculated with small errors when noise-free potential measurements are used. With an addition of noise to potential measurements, the skull is the only tissue, that is calculated accurately (except for 0.1% change). Skull and scalp can be calculated when the noise-free magnetic fields are used. If noise is added to the magnetic field measurements, conductivities for brain, CSF and scalp can be calculated with small error when the change in the conductivity is 10%.

Table 3.13: The initially assigned conductivity values increased by 0.1%, 1% and 10%.

	0.1%	1%	10%
Brain	0.2002	0.202	0.22
CSF	1.001	1.01	1.1
Skull	0.005005	0.00505	0.0055
Scalp	0.2002	0.202	0.22

Table 3.14: The calculated conductivity values. Potential difference obtained from 25 electrodes are used.

	0.1%	1%	10%
Brain	0.20018	0.2018	0.217
CSF	1.0009	1.009	1.09
Skull	0.0050054	0.0050535	0.005518
Scalp	0.20004	0.2004	0.204

Table 3.15: The calculated conductivity values. Potential difference obtained from 221 electrodes are used. A gaussian noise with a standard deviation of 10% of maximum measurement is added to the measurements.

	0.1%	1%	10%
Brain	0.183	0.191	0.219
CSF	0.971	0.994	1.066
Skull	0.0053	0.00505	0.0054
Scalp	0.188	0.185	0.194

Table 3.16: The calculated conductivity values. Magnetic fields difference obtained from 25 sensors are used.

	0.1%	1%	10%
Brain	0.20009	0.2009	0.2085
CSF	0.9999	0.9996	0.995
Skull	0.005005	0.00505	0.0055
Scalp	0.20012	0.2012	0.212

Table 3.17: The calculated conductivity values. Magnetic fields difference obtained from 25 sensors are used. A gaussian noise with a standard deviation of 10% of maximum measurement is added to the measurements.

	0.1%	1%	10%
Brain	0.202	0.218	0.2293
CSF	1.01	1.005	1.108
Skull	0.02293	0.0295	0.00897
Scalp	0.164	0.166	0.210

3.4.2 Reconstructing the conductivity distribution of the realistic head model - Many unknowns

In this section simulations similiar to Section 3.3.2, are presented for realistic head model. For this case, dimension of the sensitivity matrix is reduced to $m \times 35253$ for brain, $m \times 10877$ for CSF, $m \times 31334$ for scalp and $m \times 29143$ for skull (for magnetic fields measurements m must be replaced by $3 * m$). For EEG and MEG measurements 14 dipole sets, each having 3 dipoles at the same location (Figure 3.50) in the brain are used. The voltages are measured using 25 electrodes attached on the head surface (Figure 3.50) and magnetic fields are measured using 25 sensors placed nearby the head (Figure 3.50). Simulations are performed using noisy (A gaussian noise with a standard deviation of 10% of maximum measurement) and noise-free evoked potentials and evoked magnetic fields.

Results show that, RDM values increase with the increase in the conductivity when noise-free potentials and magnetic fields measurements are used. When noise is added to magnetic fields and potential measurements, skull is the only tissue that does not obey this monotonic increase.

Table 3.18: The computed RDM values. Potential difference obtained from 25 electrodes are used.

	0.1%	1%	10%
Brain	0.0999	0.9897	9.0718
CSF	0.0986	0.9774	8.9780
Skull	0.0956	0.9468	8.6990
Scalp	0.0904	0.8959	8.2277

Table 3.19: The computed RDM values. Potential difference obtained from 25 electrodes are used. A gaussian noise with a standard deviation of 10% of maximum measurement is added to the measurements.

	0.1%	1%	10%
Brain	0.1638	1.3112	9.0622
CSF	0.3116	1.0334	8.9836
Skull	3.19	2.2800	10.3901
Scalp	0.6197	2.2032	9.0390

Table 3.20: The computed RDM values. Magnetic fields difference obtained from 25 sensors are used.

	0.1%	1%	10%
Brain	0.1049	1.1988	10.7969
CSF	0.2019	1.8853	16.9112
Skull	0.1068	0.9098	8.3354
Scalp	0.4445	4.3999	38.3191

Table 3.21: The computed RDM values. Magnetic fields difference obtained from 221 sensors are used. A gaussian noise with a standard deviation of 10% of maximum measurement is added to the measurements.

	0.1%	1%	10%
Brain	0.9390	1.1403	9.0881
CSF	0.8693	1.0637	9.0928
Skull	42.4271	75.7418	51.7891
Scalp	6.8494	10.4935	15.8195

3.4.3 Inhomogeneity Imaging

Similar to Section 3.3.3, the goal of this section, is to investigate the performance of the adopted approach on inhomogeneity imaging. The potentials and magnetic fields are measured using the same dipole and sensor configuration similiar to the previous section. A gaussian noise with a standard deviation of 1% of maximum measurement is added to the measurements.

The effect of inhomogeneity location on the imaging performance is investigated for 5 different inhomogeneity positions (Figures 3.51, 3.56, 3.61, 3.66, 3.71) using noisy (1% of the maximum measurement is added to simulate noise) and noise-free measurements. First, the conductivity distribution of brain is reconstructed using the potential measurements without adding any noise. Figures 3.52, 3.57, 3.62, 3.67, 3.72 show that, the location of inhomogeneity is distinguished. Next, the conductivity distribution of brain is reconstructed using the potential measurements with adding noise (Figures 3.53, 3.58, 3.63, 3.68, 3.73). Although the location of the inhomogeneities are identified, there are small perturbed regions in the vicinity of the dipoles. Then, the conductivity distribution of brain is reconstructed using the magnetic fields without adding any noise. Figures 3.54, 3.59, 3.64, 3.69, 3.74 show that the location of the inhomogeneities are not distinguished accurately, because of perturbed regions in the vicinity of the inhomogeneities. Finally, the conductivity distribution of brain is reconstructed using the magnetic fields by adding noise. As the Figures 3.55, 3.60, 3.65, 3.70, 3.75 show the location of inhomogeneities can not be identified, and there are perturbations in the dipole locations.

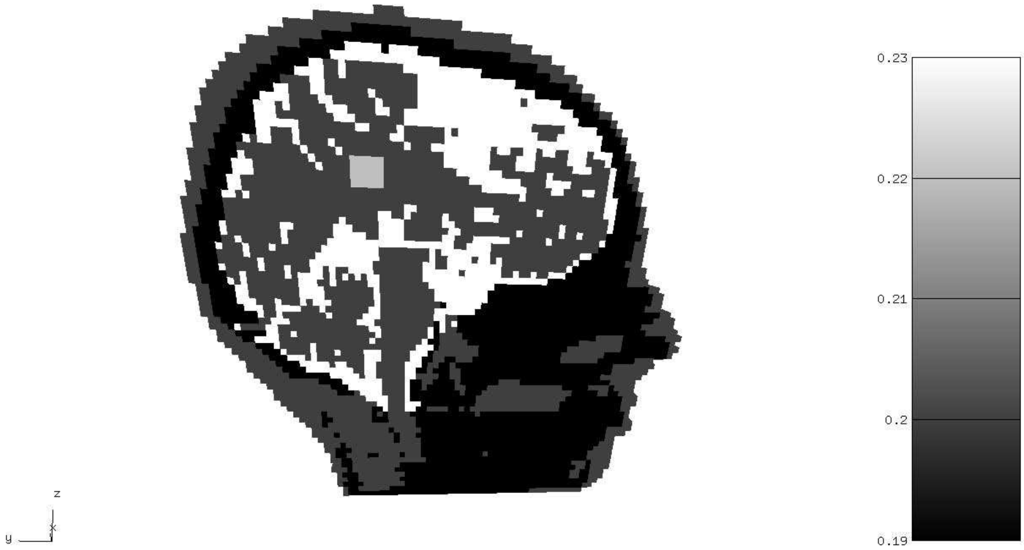

Figure 3.51: Realistic conductivity distribution of head with inhomogeneity inside (white region).

Figure 3.52: Reconstructed conductivity distribution of head with a inhomogeneity inside. Potential difference obtained from 25 electrodes are used.

Figure 3.53: Reconstructed conductivity distribution of head with a inhomogeneity inside. Potential difference obtained from 25 electrodes are used. A gaussian noise with a standard deviation of 1% of maximum measurement is added to the measurements.

Figure 3.54: Reconstructed conductivity distribution of head with a inhomogeneity inside. Magnetic fields difference obtained from 25 sensors are used.

Figure 3.55: Reconstructed conductivity distribution of head with a inhomogeneity inside. Magnetic fields difference obtained from 25 sensors are used. A gaussian noise with a standard deviation of 1% of maximum measurement is added to the measurements.

Figure 3.56: Realistic conductivity distribution of head with inhomogeneity inside (white region).

Figure 3.57: Reconstructed conductivity distribution of head with a inhomogeneity inside. Potential difference obtained from 25 electrodes are used.

Figure 3.58: Reconstructed conductivity distribution of head with a inhomogeneity inside. Potential difference obtained from 25 electrodes are used. A gaussian noise with a standard deviation of 1% of maximum measurement is added to the measurements.

Figure 3.59: Reconstructed conductivity distribution of head with a inhomogeneity inside. Magnetic fields difference obtained from 25 sensors are used.

Figure 3.60: Reconstructed conductivity distribution of head with a inhomogeneity inside. Magnetic fields difference obtained from 25 sensors are used. A gaussian noise with a standard deviation of 1% of maximum measurement is added to the measurements.

Figure 3.61: Realistic conductivity distribution of head with inhomogeneity inside (white region).

Figure 3.62: Reconstructed conductivity distribution of head with a inhomogeneity inside. Potential difference obtained from 25 electrodes are used.

Figure 3.63: Reconstructed conductivity distribution of head with a inhomogeneity inside. Potential difference obtained from 25 electrodes are used. A gaussian noise with a standard deviation of 1% of maximum measurement is added to the measurements.

Figure 3.64: Reconstructed conductivity distribution of head with a inhomogeneity inside. Magnetic fields difference obtained from 25 sensors are used.

Figure 3.65: Reconstructed conductivity distribution of head with a inhomogeneity inside. Magnetic fields difference obtained from 25 sensors are used. A gaussian noise with a standard deviation of 1% of maximum measurement is added to the measurements.

Figure 3.66: Realistic conductivity distribution of head with inhomogeneity inside (white region).

Figure 3.67: Reconstructed conductivity distribution of head with a inhomogeneity inside. Potential difference obtained from 25 electrodes are used.

Figure 3.68: Reconstructed conductivity distribution of head with a inhomogeneity inside. Potential difference obtained from 25 electrodes are used. A gaussian noise with a standard deviation of 1% of maximum measurement is added to the measurements.

Figure 3.69: Reconstructed conductivity distribution of head with a inhomogeneity inside. Magnetic fields difference obtained from 25 sensors are used.

Figure 3.70: Reconstructed conductivity distribution of head with a inhomogeneity inside. Magnetic fields difference obtained from 25 sensors are used. A gaussian noise with a standard deviation of 1% of maximum measurement is added to the measurements.

Figure 3.71: Realistic conductivity distribution of head with inhomogeneity inside (white region).

Figure 3.72: Reconstructed conductivity distribution of head with a inhomogeneity inside. Potential difference obtained from 25 electrodes are used.

Figure 3.73: Reconstructed conductivity distribution of head with a inhomogeneity inside. Potential difference obtained from 25 electrodes are used. A gaussian noise with a standard deviation of 1% of maximum measurement is added to the measurements.

Figure 3.74: Reconstructed conductivity distribution of head with a inhomogeneity inside. Magnetic fields difference obtained from 25 sensors are used.

Figure 3.75: Reconstructed conductivity distribution of head with a inhomogeneity inside. Magnetic fields difference obtained from 25 sensors are used. A gaussian noise with a standard deviation of 1% of maximum measurement is added to the measurements.

CHAPTER 4

CONCLUSION AND DISCUSSION

This thesis study introduces a novel way to reconstruct the conductivity distribution of human head using evoked fields and potentials. This approach can increase the accuracy of EMSI and can also be used to find the conductivity perturbations, i.e. inhomogeneities in the human head. Simulation results show the performance of the approach by giving numerical resuls. In this chapter, concluding comments and major contributions of the thesis study are presented.

4.1 Conclusion

4.1.1 Effect of the Number of Measurements

For a given head, the discretization for the numerical model results in N elements. If the conductivity of all these elements are unknowns, there should be N independent measurements to obtain a unique solution (assuming isotropic conductivity for each tissue type). In this study, EEG electrodes and/or MEG sensors are assumed as the means to measure the evoked responses. With the state of the art technology, the maximum number of EEG electrodes and MEG sensors can be 256, though much smaller number of electrodes (for example, 32 or 64) are usually used in practice. Thus, the required number of measurements can not be obtained at a single instant. To increase the number of independent measurements the orientation of a dipole (fixed in location) should change. Any increase in the number of sources (and their time behavior) in the ESI study will definitely increase the number of measurements, and thus the performance of the proposed study. This characteristic is shown by a number of simulation studies in this study. However, how the accuracy in ESI limits the performance of this method should be further investigated using different inverse problem algorithms developed for ESI.

In section 3.2.2, the location of an inhomogeneity is reconstructed both using a single dipole and 38 dipoles. And the results show that, while identifying the inhomogeneity is not possible with a single dipole, increase in measurements (ie, 38 dipoles) provides the correct location and size of inhomogeneity. In section 3.2.2, the measurements are increased by creating dipoles at different locations of the head model. As stated above, this is not the unique solution to increase the measurements. The other way is to set the location of a dipole fixed, and change the orientation. In section 3.2.5, the orientation of a fixed location dipole is changed 8 times, 8 indepenendet measurements are calculated. The result show that, the performance of the adopted approach increases as compared to a single measurement (ie, single dipole).

4.1.2 Contrast Resolution

Detecting a inhomogeneity in the brain at its earlist stage, even when the conductivity change is small (a perturbation) may be so critical. Therefore, the performance of the adopted approach on identification of a inhomogeneity, even for small changes, should be tested. For this purpose, in section 3.2.3, an inhomogeneity at the same location with perturbations in conductivity values are investigated. Results show that, for noise free case the conductivity value of an inhomogeneity is not so critical in finding the correct location of the inhomogeneity. When noise is introduced to the system, for an inhomogeneity with larger conductivity changes, more accurate results are obtained.

4.1.3 Computing Tissue Conductivities (4 unknowns)

Earlier in this thesis, it was stated that, for forward problem calculations mean conductivity values are assigned for tissues used in the head model. This approach might lead to inaccurate source localization problems [3] [4] [5] [6] [7] [8] [9] [10] [11]. The proposed approach is employed to compute the tissue conductivities for both concentric (section 3.3.1) and realistic (section 3.4.1) head models. Results show that, tissue conductivities are better computed using potentials measurements than using magnetic field measurements. Results, also show that, when noise is added to the measurements, using magnetic field measurements is not practical. However, when potential measurements are used, the method is more robust to the added noise and can be used to compute the tissue conductivities. For noise-free measurements, 0.1% and 1% changes in the tissue conductivities are calculated more correctly than 10% change. However, if noise is introduced to the measurements, increase in the conductivity changes yield more accurate results.

4.1.4 Reconstructing the conductivity distribution (Many unknowns)

In the previous section, the conductivity of elements within the same tissue is assumed to be uniform. As it is stated earlier that, perturbations in the conductivity distribution affect both EEG and MEG measurements [3] [12] [13] [14] [15] [16]. Therefore, the performance of the adopted approach must be investigated for the case that elements in the same tissue do not have to be uniform. For this purpose, the conductivity distribution of a tissue is reconstructed (number of unknows is the number of elements in the tissue) for both concentric (section 3.3.1) and realistic (section 3.4.1) head models. RDM is calculated to compare the reconstructed and actual conductivity distributions.

Generally, RDM values are small for small change in the conductivities. As the change in the conductivities increase the RDM value also increases.

4.1.5 Inhomogeneity Imaging

To investigate the performance of the method on inhomogeneity imaging, simulation results are presented in section 3.3.3 and 3.4.3. In this simulation studies, 5 different inhomogeneity positions for concentric and realistic head models are tried to be distinguished using potential and magnetic field measurements. Results show that, noise-free and noisy potential measurements and noise-free magnetic field measurements can be used to detect a inhomogeneity. However, using noisy magnetic field measurements for inhomogeneity detection is not possible.

4.2 Discussion

Changes in the conductivity have no effect on the primary magnetic fields for homogenous and concentric sphere head model. Moreover, changes in the secondary magnetic fields as a result of conductivity changes, are so small. Thus, reconstruction of conductivity distribution using magnetic field measurements may yield incorrect results. Potential measurements are more sensitive to volume current sources than MEG [1], and may be used for conductivity calculations

Magnetic field measurements are more sensitive to noise as compared to potential measurements. Therefore, noisy magnetic field measurements affect the conductivity calculations more strongly as compared to potential measurements. In realistic head model when noise added to MEG measurements it is seen that the location of inhomogeneity can not be detected. Instead, some conductivity perturbations appear near the dipole locations. This shows that sensitivity of MEG is more pronounced than EEG near the dipole locations.

The increase in the number of sensor and dipole leads to more accurate results. The number of sensor can be increased up to 256 for realistic reasons. However, the number of dipoles can be increased by using various external stimulus.

By using EEG measurements small changes (1%) in the conductivity distribution of the human head can be detected whenever the added noise is small or the system is noise free. However, if a noise with high amplitudes as compared to the sensor fields is added then as the change in the conductivity increases the accuracy and the performmance increases.

The location of dipoles and sensors have great importance for conductivity calculations, since sensitivity is high near the dipoles in brain and beneath the sensors in scalp [12]. If the location of dipoles is distributed in the brain more accurate results can be obtained.

The adopted approach can be used to identify conductivity and location of inhomogeneities in the human head. Considering the realistic case, MR is used to find the location of inhomogeneities, however the conductivity of the inhomogeneities can be calculated using this approach. Another application of this approach may be to find the location of an inhomogeneity when the boundary of the tissues are already obtained (i.e, the segmentation algorithms are previously applied to MR images and realistic head model for an individual is ready). In this case, it is possible to find the location of an inhomogeneity by taking EEG/MEG measurements regularly.

REFERENCES

[1] S. Baillet, J. C. Mosher, and R. M. Leahy, "Electromagnetic brain mapping," *IEEE Signal Processing Magazine*, pp. 14–30, 2001.

[2] B.He, "High-resolution source imaging of brain electrical activity," *IEEE Eng. in Med. and Biol.*, vol. 17, no. 5, pp. 123–129, 1998.

[3] C. Ramon P. H. Schimpf V. J. Wedeen J. S. George J. Haueisen, D. S. Tuch and J. W. Belliveau, "The influence of brain tissue anisotropy on human eeg and meg," *NeuroImage*, vol. 15, pp. 159–166, 2002.

[4] M. Schneider, "Effect of inhomogeneities on surface signals coming from a cerebral current dipole source," *IEEE Trans. Biomed. Eng.*, pp. 52–54, 1974.

[5] C. G. Bénar and J. Gotman, "Modeling of post-surgical brain and skull defects in the eeg inverse problem with the boundary element method," *Clin. Neur.*, vol. 113, pp. 48–56, 2002.

[6] B. M. Radich and K. M. Buckley, "EEG dipole localization bounds and map algorithms for head models with parameter uncertainties," *IEEE Trans. Bio. Eng.*, vol. 42, pp. 233–241, 1995.

[7] S. P. Van den Broek, F. Reinders, M. Donderwinkel, and M. J. Peters, "Volume conduction effects in EEG and MEG," *Electroenceph. Clin. Physiol.*, vol. 106, pp. 522–534, 1998.

[8] G. Huiskamp, M. Vroeijenstijn, R. Van Dijk, G. Wieneke, and A. C. Van Huffelen, "The need for correct realistic geometry in the inverse EEG problem," *IEEE Trans. Biomed. Eng.*, vol. 46, pp. 1281–1287, 1999.

[9] B. Vanrumste, G. Van Hoey, R. Van de Walle, M. D'Havé, I. Lemahieu, and P. Boon, "Dipole location errors in electroencephalogram source analysis due to volume conductor model errors," *Med. Biol. Eng. Comp.*, vol. 38, pp. 528–534, 2000.

[10] B. Maess R. S. Macleod C. H. Wolters, A. Anwander and A. D. Friederici, "The influence of volume conduction effects on the eeg/meg reconstruction of the sources of the early left anterior negativity," *Proceedings of the 26th Annual International Conference of the IEEE EMBS*, 2004.

[11] Carlos H. Muravchik David Gutierrez, Arye Nehorai, "Estimating brain conductivities and dipole source signals with eeg arrays," *IEEE Transactions on Biomedical Engineering*, vol. 51, no. 12, 2004.

[12] N. G. Gençer and C. E. Acar, "Sensitivity of eeg and meg measurements to tissue conductivity," *Phys. Med. Biol.*, vol. 49, pp. 701–717, 2004.

[13] N. B. Cuffin, "Eccentric spheres models of the head," *IEEE Trans. Biomed. Eng.*, vol. 38, no. 9, pp. 871–878, 1991.

[14] B. N. Cuffin, "Effects of inhomogeneous regions on electric potentials and magnetic fields: two special cases," *J. Appl. Phys.*, vol. 53, pp. 9192–9197, 1982.

[15] J. Haueisen, C. Ramon, M. Eiselt, and H. Nowak, "Influence of tissue resistivities on neuromagnetic fields and electric potentials studied with a finite element model of the head," *IEEE Trans. Biomed. Eng.*, vol. 44, pp. 727–735, 1997.

[16] C. J. Stok, "The influence of model parameters on EEG/MEG single dipole source estimation," *IEEE Trans. Biomed. Eng.*, vol. 34, pp. 289–296, 1987.

[17] J. O Ollikainen, M. Vauhkonen, P. A. Karjalainen, and J. P. Kaipio, "Effects of local skull inhomogeneities on eeg source estimation," *Med. Eng. Phys.*, vol. 21, pp. 143–154, 1999.

[18] L. A. Geddes and L. E. Baker, "The specific resistance of biological materials–a compendium of data for the biomedical engineer and physiologist," *Med. Biol. Eng.*, vol. 5, pp. 271–293, 1967.

[19] Can E. Acar, "Parallelization of the forward and inverse problems of electromagnetic source imaging of the human brain," *Ph.D. Thesis, Middle East Technical University, Ankara, Turkey*, 2003.

[20] Yoldaş Ataseven, "Parallel implementation of the boundary element method for electromagnetic source imaging of the human brain," *M.Sc. Thesis, Middle East Technical University, Ankara, Turkey*, 2005.

[21] At the 3rd National Homelessness Conference in Brisbane adapted from a speech made by Jan Bishop as President of Brain Injury Australia, "Mental illness and brain injury - fact sheet," http://braininjury.org.au/portal/fact-sheets/mental-illness-and-brain-injury—fact-sheet.html, Last accessed date: 25/08/2008.

[22] Chevon Deputy, "The relationship between epilepsy and the brain," http://serendip.brynmawr.edu/bb/neuro/neuro04/web1/cdeputy.html, Last accessed date: 25/08/2008, 2004.

[23] Robert Mathias, "Special report: Brain imaging research," *Nida Notes*, vol. 11, no. 5, 1996.

[24] J. E. Knuutila, A. I. Ahonen, M. S. Hämäläinen, M. J. Kajola, P. P. Laine, O. V. Lounasmaa, L. T. Parkkonen, J. T. Simola, and C. D. Tesche, "A 122-channel whole-cortex SQUID system for measuring the brain's magnetic fields," *IEEE Transactions on Magnetics*, pp. 3315–3320, 1993.

[25] M. S. Atkins and B. T Mackiewich, "Fully automatic segmentation of the brain in MRI," *IEEE Trans. Med. Imag.*, vol. 17, pp. 98–107, 1998.

[26] N. B. Cuffin and D. Cohen, "Magnetic fields of a dipole in special volume conductor shapes," *IEEE Trans. Biomed. Eng.*, vol. 24, no. 4, pp. 372–381, 1977.

[27] Z. Akalın and N. G. Gençer, "investigating the effects of eye conductivity on emsi forward problem using a realistic bem head model," *IEEE Trans. Biomed. Eng.*, vol. 4, no. 2, 2002.

[28] D. C. Barber and B. H. Barber, "Applied potential tomography," *J. Phys. E. Sci. Instrum.*, vol. 17, pp. 723–733, 1984.

[29] B. H. Brown, "Medical impedance tomography and process impedance tomography: a brief review," *Meas. Sci. Technol.*, vol. 12, pp. 991–996, 2001.

[30] M. Kuzuoğlu N. G. Gençer and Y. Z. Ider, "Electrical impedance tomography using induced currents," *IEEE Trans. Medical Imaging*, vol. 13, no. 2, pp. 338–350, 1994.

[31] I.L. Freeston J.M. Scaife, R.C. Tozer, "Conductivity and permittivity images from induced current electrical impedance tomography system," *IEE Proc.-Sci. Meas. Technol*, vol. 141, no. 5, pp. 356–362, 1994.

[32] I.L. Freeston and R.C. Tozer, "Impedance imaging using induced currents," *Physiol. Meas.*, vol. 16, pp. A257–A266, 1995.

[33] E.Forner J.Netz and S.Haagemann, "Contactless impedance measurement by magnetic induction- a possible method for investigation of brain impedance," *Physiol. Meas.*, vol. 14, pp. 463–471, 1993.

[34] M. N. Tek N. G. Gençer, "Forward problem solution for electrical conductivity imaging via contactless measurements," *Phys. Med. Biol.*, vol. 44, pp. 927–940, 1999.

[35] M. N. Tek N. G. Gençer, "Electrical conductivity imaging via contactless measurements," *IEEE Transactions on Medical Imaging*, vol. 18, pp. 617–627, 1999.

[36] W.R. Stewart H.Griffiths and W.Gough, "Magnetic induction tomography. a measuring system for biological tissues," *Ann. N Y Acad. Sci.*, vol. 873, pp. 335–345, 1999.

[37] A.V. Korjenevsky and V.A. Cherepenin, "Progress in realization of magnetic induction tomography," *Ann. N Y Acad. Sci.*, vol. 873, pp. 346–352, 1999.

[38] V.Cherepenin A.Korjenevsky and S.Sapetsky, "Magnetic induction tomography: Experimental realization," *Physiol. Meas.*, vol. 21, pp. 89–94, 2000.

[39] H.Griffiths, "Magnetic induction tomography," *Meas. Sci. Technol*, vol. 12, pp. 1126–1131, 2001.

[40] H.Lackner H.Scharfetter and J.Rosell, "Magnetic induction tomography: Hardware for multi-frequency measurements in biological tissues," *Physiol. Meas.*, vol. 22, pp. 131–146, 2001.

[41] B.M. Eyuboglu Ozlem Birgul and Y.Z. Ider, "Experimental results for 2d magnetic resonance- electrical impedance tomography (mr-eit) using magnetic flux density in one direction," *Physics in Medicine and Biology*, vol. 48, no. 21, pp. 3485–3504, 2003.

[42] O. Ozbek M.S. Ozdemir, B. M. Eyuboglu, "Equipotential projection based magnetic resonance - electrical impedance tomography and experimental realisation," *Physics in Medicine and Biology*, vol. 49, no. 20, pp. 4765–4783, 2004.

[43] Y. Z. Ider L.Ozparlak, "Induced current magnetic resonance-electrical impedance tomography," *Physiol Meas.*, vol. 26, pp. 289–305, 2005.

[44] B.M. Eyuboglu Ozlem Birgul and Y.Z. Ider, "Current constraint voltage scaled reconstruction (ccvsr) algorithm for mr-eit and its application with different probing current patterns," *Physics in Medicine and Biology*, vol. 48, no. 5, pp. 653–671, 2003.

[45] Paul. L. Nunez, "A method to estimate local skull resistance in living subjects," *IEEE Trans. Biomed. Eng.*, vol. 34, no. 11, 1987.

[46] Ugur Baysal and Jens Haueisen, "Use of a priori information in estimating tissue resistivities- application to human data in vivo," *Physiol. Meas.*, vol. 25, no. 3, pp. 737–748, 2004.

[47] Satish Balay, Kris Buschelman, William D. Gropp, Dinesh Kaushik, Matt Knepley, Lois Curfman McInnes, Barry F. Smith, and Hong Zhang, "Petsc users manual," Tech. Rep. ANL-95/11 - Revision 2.1.5, Argonne National Laboratory, 2002.

[48] Satish Balay, Kris Buschelman, William D. Gropp, Dinesh Kaushik, Matt Knepley, Lois Curfman McInnes, Barry F. Smith, and Hong Zhang, "Petsc home page," http://www.mcs.anl.gov/petsc, Last accessed date: 25/08/2008.

[49] Satish Balay, William D. Gropp, Lois Curfman McInnes, and Barry F. Smith, "Efficient management of parallelism in object oriented numerical software libraries," in *Modern Software Tools in Scientific Computing*, E. Arge, A. M. Bruaset, and H. P. Langtangen, Eds. 1997, pp. 163–202, Birkhauser Press.

[50] T.F. Chan J. Demmel J. Donato J. Dongarra V. Eijkhout R. Pozo C. Romine H. Van der Vorst R. Barrett, M. Berry, "Templates for the solution of linear systems: Building blocks for iterative methods, 2nd ed.," http://www.netlib.org/linalg, Last accessed date: 25/08/2008.

[51] Guofa Shou Mingfeng Jiang, Ling Xia and Min Tang, "Combination of the lsqr method and a genetic algorithm for solving the electrocardiography inverse problem," *Phys. Med. Biol.*, vol. 52, pp. 1277–1294, 2007.

[52] M.E. Kilmer and D.P. OLeary, "Choosing regularization parameters in iterative methods for ill-posed problems," *SIAM J. Matrix Anal. Appl.*, vol. 22, pp. 1204, 2001.

[53] N. Valdivia and E.G. Williams, "Krylov subspace iterative methods for boundary element method based near-field accustic holography," *J. Acoust. Soc. Am.*, vol. 117, pp. 711, 2005.

[54] O. Menchi P. Brianzi, P. Favati and F. Romani, "A framework for studying the regularizing properties of krylov subspace methods inverse problems," *Institute of Physics, Bristol, ROYAUME-UNI*, vol. 22, pp. 1007, 2006.

[55] G.H. Golub and W. Kahan, "Calculating the singular values and pseudoinverse of a matrix," *SIAM J. Numer. Anal.*, vol. 2, pp. 205, 1965.

[56] Christopher C. Paige and Michael A. Saunders, "Lsqr:an algorithm for sparse linear equations and sparse least squares," *ACM Trans. Math. Softw. 8*, vol. 2, 1982.

[57] Gerald Matz Franz Hlawatsch Georg Tauböck, Mario Hampejs and Karlheinz Gröchenigb, "Lsqr-based ici equalization for multicarrier communications in strongly dispersive and highly mobile environments," *IEEE Signal Processing Advances in Wireless communications*, p. 1, 2007.

APPENDIX A

FORWARD PROBLEM FORMULATION

In this section, derivation of forward problem equations will be given briefly. The formulations presented here were derived previously [19] and interested readers can look up that study for further information.

The potential and magnetic fields must satisfy the following equations

$$\begin{aligned} \nabla \cdot (\sigma \nabla \phi) &= \nabla \cdot J^i \quad \textit{inside } V \\ \sigma \frac{\partial \phi}{\partial n} &= 0 \qquad\quad \textit{on } S \end{aligned} \tag{A.1}$$

and

$$\begin{aligned} \nabla^2 B &= -\mu_0 \nabla \times J \\ B &= 0 \qquad\quad \text{at infinity} \end{aligned} \tag{A.2}$$

where J^i is the current density, J is the total current density, ϕ is the potential field, B is magnetic field, σ is the conductivity distribution, μ_0 is the permeability of free space, n is the unit normal, V is the volume and S is the surface of the conducting body.

After ϕ is found, total current density is calculated as follows:

$$J = J^i - \sigma \nabla \phi \tag{A.3}$$

and the magnetic field B is calculated using the the Biot-Savart Law:

$$B(r) = \frac{\mu_0}{4\pi} \int_{V'} J^i(r') \times \frac{R}{R^3}\, dV' - \frac{\mu_0}{4\pi} \int_{V'} \sigma(r') \nabla \phi(r') \times \frac{R}{R^3}\, dV' \tag{A.4}$$

where $R = r - r'$ is the vector between the field and source points.

For solving the forward problem of EMSI, the above formulas must be discretized using FEM. The aim in FEM is to divide the conducting body into elements such that conductivity and potential is constant throughout in each element. The potential on the specified element can be found by interpolation of node voltages of that element as follows:

$$f(\xi,\zeta,\eta)=\sum_{i=1}^{k}N_i(\xi,\zeta,\eta)f_i \tag{A.5}$$

where f is the potential function, (ξ,ζ,η) are the *local* coordinates inside the element, k is the number nodes of an element and $N_i(\xi,\zeta,\eta)$ is the shape function. For each element used in the head model, both sides of Equation (A.1) is multiplied with a shape function. And it is integrated throughout the element volume:

$$\int_{V_e} N_i\nabla\cdot(\sigma_e\nabla\Phi)dV_e=-\int_{V_e} N_i\nabla\cdot J_e^i\, dV_e \quad i=1...k \tag{A.6}$$

where for an element e, k is the number of nodes, V_e is the volume, σ_e is the conductivity, J_e^i is the impressed current density. After using appropriate vector identities and Gauss' theorem,

$$\int_{V_e}\sigma_e\nabla N_i\cdot\nabla\Phi dV_e=\int_{S_e}N_i\sigma_e\nabla\Phi\cdot dS_e-\int_{V_e}N_i\nabla\cdot J_e^i\, dV_e \tag{A.7}$$

is obtained, where dS_e is the outward directed differential surface element. Since $\sigma\frac{\partial\Phi}{\partial n}=-J_e^i\cdot n$ on every element surface, equation (A.7) becomes:

$$\int_{V_e}\sigma_e\nabla N_i\cdot\nabla\Phi dV_e=\int_{S_e}N_iJ_e^i\cdot dS_e \tag{A.8}$$

Φ can be calculated using the node potential. For this purpose if Equation (A.5) is used, the following will be obtained:

$$\nabla\Phi=\sum_{j=1}^{k}(\nabla N_j)\Phi_j^e \tag{A.9}$$

By combining Equation (A.8) and Equation (A.9) and remembering divergence of constant current density in an element is zero, the following will be obtained:

$$\sum_{j=1}^{k}\left(\int_{V_e}\sigma_e\nabla N_i\cdot\nabla N_j\, dV_e\right)\Phi_j^e=\int_{S_e}N_iJ_e^i\cdot dS_e \tag{A.10}$$

This yields $k\times k$ local element matrix for the element. And if these local element matrices are assembled, the linear system of equations are obtained as follows:

$$A(\sigma)\Phi=b \tag{A.11}$$

where for l nodes and n elements A is $l \times l$ matrix (contains element geometry and conductivity information), Φ is an $l \times 1$ unknown node potentials vector, σ is the $n \times 1$ element conductivities vector, After Φ is solved the magnetic field B is obtained using the following equation:

$$\begin{aligned} B(r) &= \frac{\mu_0}{4\pi} \int_{V'} J^i r') \times \frac{R}{R^3} dV' \\ &- \frac{\mu_0}{4\pi} \sum_j \int_{S_j} \Delta\sigma_j \Phi(r') \frac{R}{R^3} \times dS'_j \end{aligned} \tag{A.12}$$

where $\Delta\sigma_j$ is the conductivity difference across the boundary of the j^{th} conductivity region in the direction of dS_j. This expression is discretized as following:

$$\begin{aligned} B(r) &= \frac{\mu_0}{4\pi} \sum_{j=1}^{n} \int_{V_j} (J^i)_j \times \frac{R_j}{(R_j)^3} dV_j \\ &+ \frac{\mu_0}{4\pi} \sum_{j=1}^{n} \int_{S_j} \sigma_j \Phi \frac{R_j}{(R_j)^3} \times dS_j \end{aligned} \tag{A.13}$$

where V_j and S_j represent volume and surface of the j^{th} element and $(J^i)_j$ is the primary current defined on the j^{th} element.

The matrix form of the above integrations is as follows:

$$B^e = B_0^e + C(\sigma)^e \Phi(\sigma)^e \tag{A.14}$$

where B^e and B_0^e are $C(\sigma)^e$ are $3s \times 1$ vectors and $C(\sigma)^e$ is a $3s \times k$ matrix.

Equation A.14 is written for each element and after that, the matrix equations are assembled and finally the following equation is obtained:

$$B = B_0 + C(\sigma)\Phi(\sigma) \tag{A.15}$$

APPENDIX B

DERIVATION OF SENSITIVITY MATRIX

In this section, derivation of sensitivity matrix for both EEG and MEG will be given briefly. The formulations presented here were derived previously [19] and interested readers can look up that study for further information.

B.0.1 EEG

The aim in sensitivity analysis is to relate change in the potentail with change in the conductivity. For this purpose two mathematical expressions can be written using forward problem formulation:

$$\nabla.(\sigma_0 \nabla \phi_0) = \nabla.J^i \tag{B.1}$$

$$\nabla.(\sigma \nabla \phi) = \nabla.J^i \tag{B.2}$$

where J^i is the current density, σ_0 is the initially assigned conductivity distributions, σ is the perturbed conductivity distributions, ϕ_0 and ϕ are the potential distributions for σ_0 and σ.

If Equation (B.2) is rewritten by substituting $\phi_0 + \Delta\phi$ and $\sigma_0 + \Delta\sigma$ for ϕ and σ then the following equation will be obtained:

$$\nabla \cdot [\sigma_0 \nabla \phi_0 + \sigma_0 \nabla(\Delta\phi) + \Delta\sigma \nabla \phi_0 + \Delta\sigma \nabla(\Delta\phi)] = \nabla \cdot J^i \tag{B.3}$$

If the second order variation is neglected, the following equation will be obtained:

$$\nabla \cdot (\sigma_0 \nabla(\Delta\phi)) \quad = \quad -\nabla \cdot (\Delta\sigma \nabla \phi_0) \tag{B.4}$$

If Equation (B.4) is rewritten by substituting $\sigma - \sigma_0$ for $\Delta\sigma$ and discretized as similiar to the forward problem case then following two formulations will be obtained:

$$\nabla \cdot (\sigma_0 \nabla(\Delta\phi)) = -\nabla \cdot (\sigma\nabla\phi_0) - \nabla \cdot (\sigma_0\nabla\phi_0) \tag{B.5}$$

$$A(\sigma_0)\Delta\Phi = -(A(\sigma)\Phi_0 - A(\sigma_0)\Phi_0) \tag{B.6}$$

If the right-hand-side of this equation is expressed as a linear approximation around an initial conductivity σ_0, then following equation can be written:

$$A(\sigma_0)\Delta\Phi = -\frac{\partial}{\partial\sigma}(A(\sigma)\Phi_0)\Big|_{\sigma=\sigma_0}\Delta\sigma \tag{B.7}$$

$$\Delta\Phi = -A(\sigma_0)^{-1}\frac{\partial}{\partial\sigma}(A(\sigma)\Phi_0)\Big|_{\sigma=\sigma_0}\Delta\sigma \tag{B.8}$$

Equation (B.8) needs more modifications to reduce the complexity of taking the inverse of matrix A. Since only the potentials at the sensor nodes are required, it is sufficient to take the inverse of LA^{-1} where L is the $n \times k$ sparse matrix that selects n sensors out of k nodes. Then, both side of the equation is multiplied with L and the following is obtained:

$$\Delta\Phi_s = -LA(\sigma_0)^{-1}\frac{\partial}{\partial\sigma}(A(\sigma)\Phi_0)\Big|_{\sigma=\sigma_0}\Delta\sigma \tag{B.9}$$

$$\Delta\Phi_s = S_\Phi\Delta\sigma \tag{B.10}$$

where $\Phi_s = L\Phi$ and S_Φ is the sensitivity matrix for the voltage measurements.

B.0.2 MEG

Sensitivity of MEG measurements to conductivity perturbations start with the following two formulas:

$$B_s(\sigma_0) = \frac{\mu_0}{4\pi}\int \sigma_0\nabla\phi_0 \times \frac{R}{R^3}\,dV' \tag{B.11}$$

$$B_s(\sigma) = \frac{\mu_0}{4\pi}\int \sigma\nabla\phi \times \frac{R}{R^3}\,dV' \tag{B.12}$$

where $B_s(\sigma_0)$ and $B_s(\sigma)$ are secondary magnetic fields for σ_0 and σ. The primary magnetic fields are not taken into the formulations since they are independent of conductivity distribution.

If Equation (B.12) is rewritten by substituting $\phi_0 + \Delta\phi$ and $\sigma_0 + \Delta\sigma$ for ϕ and σ then the following equation will be obtained:

$$\begin{aligned} B_s(\sigma_0 + \Delta\sigma) &= \frac{\mu_0}{4\pi}\int (\sigma_0 + \Delta\sigma)\nabla(\phi_0 + \Delta\phi) \times \frac{R}{R^3}\, dV' \qquad \text{(B.13)} \\ &= \frac{\mu_0}{4\pi}\int \Big[\sigma_0\nabla\phi_0 + \sigma_0\nabla(\Delta\phi) + \Delta\sigma\nabla\phi_0 + \Delta\sigma\nabla(\Delta\phi)\Big] \times \frac{R}{R^3}\, dV' \end{aligned}$$

Again omitting the second order variation $(\Delta\sigma\nabla(\Delta\phi))$ and remembering $B_s(\sigma_0 + \Delta\sigma) = B_s(\sigma_0) + \Delta B$, the following equation is obtained:

$$\Delta B = \frac{\mu_0}{4\pi}\int \Big[\sigma_0\nabla(\Delta\phi) + \Delta\sigma\nabla\phi_0\Big] \times \frac{R}{R^3}\, dV \qquad \text{(B.14)}$$

If $\sigma - \sigma_0$ for $\Delta\sigma$ is substituted for $\Delta\sigma$ in Equation (B.14) and after discretized like EEG, the following will be obtained:

$$\Delta B = C(\sigma_0)\Delta\Phi + (C(\sigma)\Phi_0 - C(\sigma_0)\Phi_0) \qquad \text{(B.15)}$$

If the second term on the right-hand-side of this equation is expressed as a linear approximation around an initial conductivity distribution σ_0 then:

$$\Delta B = C(\sigma_0)\Delta\Phi + \frac{\partial}{\partial\sigma}(C(\sigma)\Phi_0)\Big|_{\sigma=\sigma_0} \Delta\sigma \qquad \text{(B.16)}$$

By combining Equation (B.8) and Equation (B.16), the following will be obtained:

$$\begin{aligned} \Delta B &= \Bigg[\frac{\partial}{\partial\sigma}(C(\sigma)\Phi_0)\Big|_{\sigma=\sigma_0} \\ &- C(\sigma_0)A(\sigma_0)^{-1}\frac{\partial}{\partial\sigma}(A(\sigma)\Phi_0)\Big|_{\sigma=\sigma_0}\Bigg]\Delta\sigma \qquad \text{(B.17)} \\ \Delta B &= S_B\Delta\sigma \qquad \text{(B.18)} \end{aligned}$$